

RESEARCH ARTICLE

Morphogenetic control of zebrafish cardiac looping by Bmp signaling

Verónica A. Lombardo^{1,2,*}, Melina Heise^{3,*}, Motahareh Moghtadaei^{3,4}, Dorothee Bornhorst^{3,4}, Jörg Männer⁵ and Salim Abdelilah-Seyfried^{3,4,‡}

ABSTRACT

Cardiac looping is an essential and highly conserved morphogenetic process that places the different regions of the developing vertebrate heart tube into proximity of their final topographical positions. High-resolution 4D live imaging of mosaically labelled cardiomyocytes reveals distinct cardiomyocyte behaviors that contribute to the deformation of the entire heart tube. Cardiomyocytes acquire a conical cell shape, which is most pronounced at the superior wall of the atrioventricular canal and contributes to S-shaped bending. Torsional deformation close to the outflow tract contributes to a torque-like winding of the entire heart tube between its two poles. Anisotropic growth of cardiomyocytes based on their positions reinforces S-shaping of the heart. During cardiac looping, bone morphogenetic protein pathway signaling is strongest at the future superior wall of the atrioventricular canal. Upon pharmacological or genetic inhibition of bone morphogenetic protein signaling, myocardial cells at the superior wall of the atrioventricular canal maintain cuboidal cell shapes and S-shaped bending is impaired. This description of cellular rearrangements and cardiac looping regulation may also be relevant for understanding the etiology of human congenital heart defects.

KEY WORDS: BMP, Wnt, Cardiac looping, Hemodynamics, Zebrafish

INTRODUCTION

The term ‘cardiac looping’ defines a morphogenetic process during vertebrate heart development that brings the developing heart chambers into an approximation of their definitive topographical relationships. This involves the transformation of an initially straight heart tube into a curved and S-shaped loop that is asymmetrically positioned along the left/right (L/R) body axis (Männer, 2000, 2009; Patten, 1922). In higher vertebrates, cardiac looping comprises several sub-processes (Männer, 2000, 2009): (1) ventricular bending along the mid-sagittal body plane causes the heart tube to acquire a C-shape with a convexity that is most pronounced along the original ventral midline of the heart tube; (2) ventricular rotation/torsion around the longitudinal axis of the heart tube leads to a helical deformation of the ventricular bend and

to dextral heart looping (ventricular D-looping) along the L/R body axis (Männer, 2004); (3) displacements of embryonic heart segments along the cranio-caudal body axis due to a shortening of the distance between the venous and arterial poles, and a displacement of the ventricular bend from its original position cranial to the atria towards its definitive position caudal to the atria; and (4) ‘untwisting’ or ‘terminal repositioning’ results in a partial rewinding of the rightward-most rotation/torsion of the heart loop (Männer, 2009; Singleman and Holtzman, 2012).

Given the morphogenetic complexity of this process, it is not surprising that animal models for human congenital heart defects frequently show abnormal heart looping during early embryonic development (Ramsdell, 2005). Yet our understanding of molecular mechanisms involved in cardiac looping still remains fragmentary. For example, signaling by Nodal (Chen et al., 2010; Grimes and Burdine, 2017) or bone morphogenetic protein (BMP) is essential for asymmetric positioning of the heart loop along the L/R body axis (Breckenridge et al., 2001; Chen et al., 1997; Chocron et al., 2007; Ocaña et al., 2017; Smith et al., 2008; Veerkamp et al., 2013; Zhang and Bradley, 1996), but much less is known about how cardiac L/R asymmetry is determined during looping morphogenesis. In mouse and zebrafish mutants with defective L/R asymmetry due to a loss of Nodal signaling, the transformation of a linear heart tube into an S-shaped heart loop is not affected. However, its orientation along the L/R body axis is randomized, with 50% of mutants displaying the normal ventricular bend (D-loop), while the remainder forms an abnormal L-loop (Baker et al., 2008; Brennan et al., 2002). Similarly, it is unknown whether disturbed Bmp pathway signaling directly causes defective looping morphogenesis or whether such defects are secondary to its earlier roles (Breckenridge et al., 2001).

Both, organ-intrinsic and organ-extrinsic factors have been proposed for regulating cardiac looping morphogenesis (Männer, 2000; Taber, 2006). The strongest evidence for the presence of intrinsic factors stems from the observation that isolated embryonic hearts, explanted at linear heart tube stages and cultured *in vitro*, still acquire C-shaped and S-shaped morphologies (Bacon, 1945; Butler, 1952; Latacha et al., 2005; Manning and McLachlan, 1990; Noël et al., 2013). Pharmacological inhibition of the actomyosin network suggested that cytoskeleton-driven changes in cell shapes and intrinsic cell chirality may drive intrinsic heart tube bending (Latacha et al., 2005; Noël et al., 2013). External factors that impact cardiac looping could be hemodynamic forces exerted by blood flow. In zebrafish, blood flow triggers the elongation of ventricular cells within the outer curvature (Auman et al., 2007). Similar anisotropic cell growth has also been described during cardiac looping in other vertebrates (Kidokoro et al., 2008; Manasek et al., 1972; Shi et al., 2014a; Soufan et al., 2006; Voronov et al., 2004). However, in lung-breathing vertebrates, cardiac looping is not compromised in the absence of blood flow, indicating that hemodynamic forces do not play a significant role (Abu-Day

¹Instituto de Biología Molecular y Celular de Rosario, Consejo Nacional de Investigaciones Científicas y Técnicas and Universidad Nacional de Rosario, 2000 Rosario, Argentina. ²Centro de Estudios Interdisciplinarios, Universidad Nacional de Rosario, 2000 Rosario, Argentina. ³Institute of Molecular Biology, Hannover Medical School, D-30625 Hannover, Germany. ⁴Institute of Biochemistry and Biology, Potsdam University, D-14476 Potsdam, Germany. ⁵Institute of Anatomy and Embryology, UMG, Göttingen University, D-37075 Göttingen, Germany. *These authors contributed equally to this work

‡Authors for correspondence (salim.seyfried@uni-potsdam.de; lombardo@ibr-conicet.gov.ar)

© V.A.L., 0000-0002-2042-3372; S.A.-S., 0000-0003-3183-3841

et al., 2009; Fransen and Lemanski, 1988; Manasek and Monroe, 1972). Another extrinsic factor contributing to cardiac looping could be mechanical forces due to restraints by surrounding tissues. In zebrafish, myocardial chamber size increases mainly due to the accretion of second heart field (SHF)-derived cardiomyocyte progenitor cells to both ends of the heart tube (de Pater et al., 2009; Hami et al., 2011; Zhou et al., 2011). Model simulations suggest that a continuous elongation of the heart tube within a tissue-confined space such as the pericardial cavity could ultimately result in the morphological changes observed during heart looping (Bayraktar and Männer, 2014). To functionally understand the contributions of different morphogenetic processes during cardiac looping morphogenesis, tractable genetic models are required.

Here, we describe the process of cardiac S-looping morphogenesis in the zebrafish embryo and identify three distinct cell- and tissue-scale transformations that all contribute to this process. We recognize BMP signaling as an important tissue-intrinsic regulator of cardiac bending at the AVC region of the heart tube. We also find that BMP signaling has a regional patterning that correlates with bending of the nascent heart tube and is maintained in the absence of Nodal signaling. These results provide novel insights into the molecular control of cardiac looping morphogenesis in the zebrafish, with relevance for a more comprehensive understanding of human congenital heart defects.

RESULTS

Zebrafish cardiac morphogenesis involves early and advanced S-looping phases

In zebrafish, cardiac looping morphogenesis becomes apparent between 30 and 54 h post fertilization (hpf). To analyze cardiac morphologies during looping stages, we used the transgenic reporter line *Tg(myl7:EGFP)^{twu34}*, which labels myocardial cells, and extracted hearts at 30, 36, 42, 48 and 54 hpf (Fig. 1A-E). Based on two-dimensional projections of confocal *z*-scans of these hearts (Fig. 1A-E), cardiac looping morphologies can be divided into an ‘early S-looping’ phase, between 30 and 42 hpf (Fig. 1A-C) and an ‘advanced S-looping’ phase, between 42 and 54 hpf (Fig. 1D,E). Early S-looping involves ventricular D-bending along the outer curvature and atrial bending with an outer curvature towards the left. Advanced S-looping involves a cranial shift of the atrium and, as a consequence, the two heart chambers are positioned side-by-side and their convex curvatures become prominent (Fig. 1E). This coincides with an angulation of the heart at the AVC, which is a useful measure for the extent of S-looping (see below). Simultaneously with advanced S-looping, the heart chamber volumes expand anisotropically along their outer curvatures in a process referred to as cardiac ballooning (Bakkers, 2011; Christoffels et al., 2000). In addition, while cardiac looping progresses, the heart shifts from a left-sided body position at heart tube stages (around 30 hpf) to a cranial-ventral position at advanced S-looping stages (>48 hpf). At ballooning stages (54 hpf), the two heart chambers, ventricle on the right and atrium on the left, are positioned in a single plane perpendicular to the mid-sagittal body plane (Fig. 1F). Hence, the deformation of the linear heart tube into an S-shaped loop resembles ‘planar bending’ of the two heart chambers into opposite directions.

Cardiac S-looping coincides with planar bending, torsional winding and anisotropic ballooning

These findings suggest that the S-shaped morphology of the embryonic zebrafish heart results from at least two independent processes: planar bending and anisotropic ballooning of both

chambers. To further characterize these morphogenetic processes, we developed quantitative methods to: (1) precisely measure the extent of planar bending; (2) analyze regional changes in shape, size and position of myocardial cells that may contribute to S-looping; and (3) quantify the process of cardiac torsion. This analysis would also clarify whether torsion of the heart, similar to cardiac looping in lung-breathing vertebrates, may also occur in zebrafish. First, we analyzed the extent of cardiac planar bending during S-looping stages based on two independent morphometric measurements. Shown is the looping angle (α) (as defined in the Materials and Methods section) (Fig. 1G). Using this method, we measured a looping angle of $85\pm 4^\circ$ for wild-type hearts at 54 hpf, which shows that the midline of the heart bends almost at a right angle (Fig. 1G,H; Table S1). As a second parameter for cardiac bending, we compared the distance between atrial and ventricular apex (*b*) with the entire length of the heart (*a*) (see scheme in Fig. 1I for a more detailed explanation). The index value (*a/b*) is inversely proportional to the extent of chamber overlap. Thus, the index value (*a/b*) decreases while S-looping progresses. By this method, we measured a looping overlap of 2.2 ± 0.2 for wild-type hearts at 54 hpf (Fig. 1J; Table S1). Hence, the index value (*a/b*) correlates with the shortening of the total length of the heart (*a*) relative to the increasing region of chamber overlap (*b*).

In lung-breathing vertebrates, cardiac looping involves a rotation/torsion of the heart tube along its longitudinal axis, which is responsible for asymmetric positioning of the ventricular bend along the L/R body axis and for its helical deformation (Männer, 2000, 2009; Taber et al., 2010; Voronov et al., 2004). Torsion may also contribute to looping of the zebrafish heart (Weber et al., 2017). Hence, we performed multi-color mosaic labeling of cardiomyocytes combined with high-resolution 4D confocal microscopy to assess the exact three-dimensional changes that occur during zebrafish cardiac looping morphogenesis. To unambiguously identify cardiomyocytes, fertilized eggs carrying the transgenic *Tg(myl7:EGFP)^{twu34}* reporter were injected with a mixture of *myl7:TagRFP-T* and *myl7:TagBFP* constructs (Staudt et al., 2014). This resulted in a mosaic expression of fluorescently colored cardiomyocytes due to random combinations and varying expression levels of the three fluorescent proteins. Based on this approach, we identified cell positions and morphologies of individual cardiomyocytes, which were monitored *in vivo* during cardiac advanced S-looping stages (40–54 hpf) (Fig. 1K, top panel). To quantify torsional winding of the heart tube, we assessed whether mosaically labelled cross-section planes derived from high-resolution reconstructions of stacks of confocal *z*-scans were angularly shifted relative to other section planes over time along the heart tube (Fig. 1K, bottom panel; see color-coded arrowheads and dotted lines, top panel). In total, three individual section planes with an even distribution along the heart were selected in each chamber (Fig. 1K, top panel). First, all cross-section planes at 40 and 54 hpf stages were normalized according to their respective geometric orientation at 48 hpf (Fig. S1A); this provided the necessary spatial reference for determining angular shifts (ρ) within each section plane. Within the selected section planes, we identified individual cells at different time points (40, 48 and 54 hpf) by taking advantage of their mosaic color labeling (Fig. S1B) and determined the angular position of each of these uniquely labeled cells relative to the midline (Fig. S1C) (cells that were not identified at each of the three time points were not considered in this analysis). Then angular shifts for a specific time window (40–48 hpf, 48–54 hpf and 40–54 hpf) were calculated by subtracting the angular positions (θ) of all cells for t_2-t_1 (with t_1 =earlier stage) (Fig. S1D; Fig. 1L with a representative angular shift measurement of cross-section plane 1 between 40 and 54 hpf).

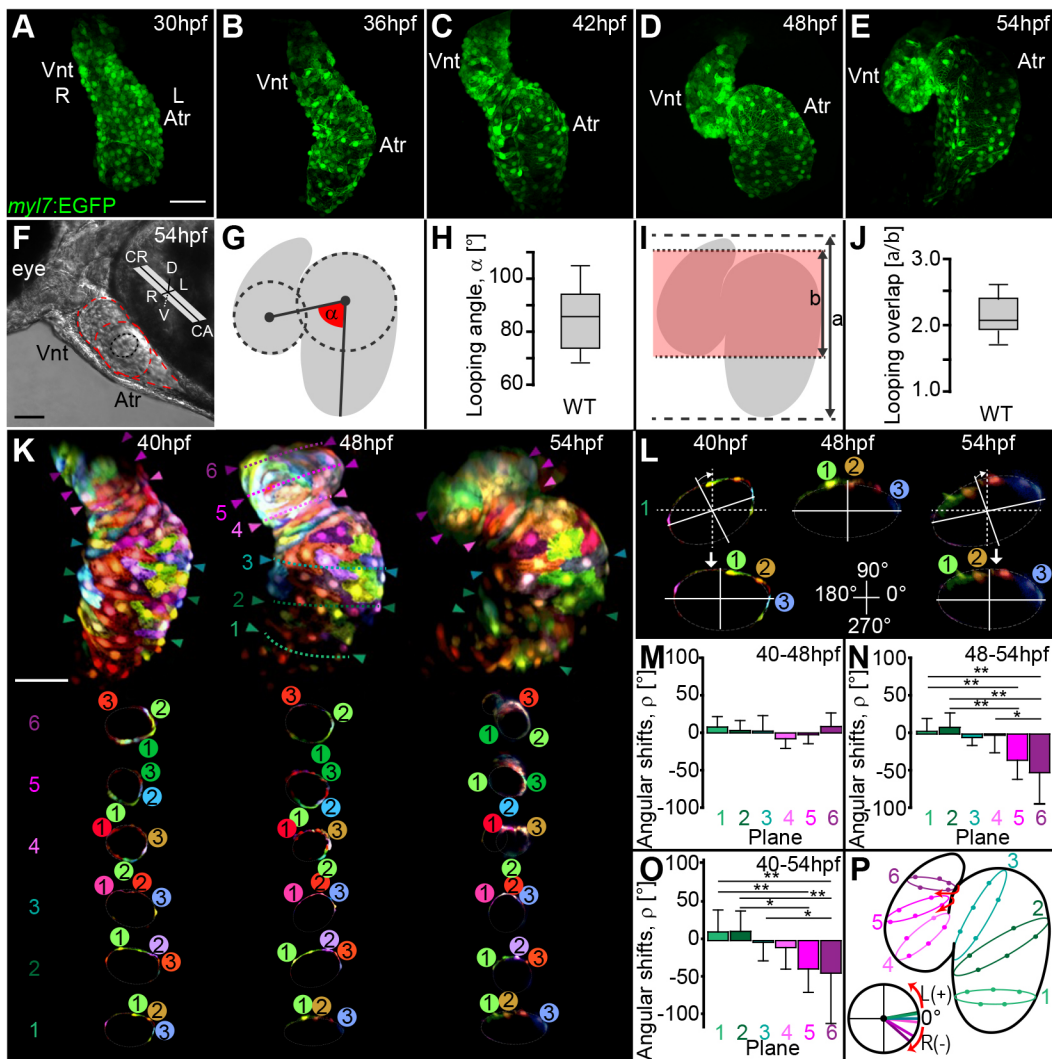


Fig. 1. Zebrafish cardiac S-looping involves planar bending and torsional winding of the heart tube. (A-E) Reconstructions of confocal z-stacks of representative wild-type hearts expressing EGFP within myocardial tissue [*Tg(myl7:EGFP)^{twu34}*] during cardiac looping stages at 30–54 hpf. (A–C) Early S-looped hearts and (D,E) advanced S-looped hearts. (F) Light microscopic image showing the positioning of the heart within the embryonic body axes at 54 hpf. (G,I) Schematic models illustrating how ‘heart bending extension’ was quantified at 54 hpf. (G) Scheme of looping angle (α , red angle). (I) The index a/b (red shading indicates overlap of heart chambers). (H,J) Looping angles (α) and index a/b of wild-type hearts at 54 hpf. The limits of the boxes indicate the range between the first quartile (25th percentile) and the third quartile (75th percentile). The line inside box indicate the median value. The error bars indicate the maximum and minimum values. (K–P) Zebrafish cardiac looping morphogenesis involves torsion of the heart. (K) Reconstruction of confocal z-scan images taken from a time series (40–54 hpf). *In vivo* multi-color mosaic-labeling based on 1- to 4-cell stage plasmid injections into *Tg(myl7:EGFP)^{twu34}* transgenic zebrafish (false-colored red). At least three myocardial cells within each cross-section plane were tracked during looping morphogenesis. One reference plane was used to ensure the consistent orientation of the imaged hearts at 40, 48 and 54 hpf. (L) Representative angular realignment of cross-section plane 1. Cross-section planes at 40 and 54 hpf were reoriented to align with the orientation of the cross-section plane at 48 hpf. Angular shifts (ρ) for each plane were calculated based on these realignments. (M–O) Quantifications of the heart torsion based on calculations of ρ for each cross-section plane occurring during (M) 40–48 hpf, (N) 48–54 hpf and (O) 40–54 hpf. (P) Schematic representation showing right-angular shifts [R(–)] close to the outflow tract of the ventricle (planes 5 and 6). All values are mean \pm s.d. (Table S2A); * $P \leq 0.05$; ** $P \leq 0.01$ (Table S2B). Atr, atrium; Vnt, ventricle; CR, cranial; CA, caudal; D, dorsal; V, ventral; L, left; R, right; L(+), left-angular shift; R(–), right angular shift. Scale bars: 50 μ m in A–E,K; 100 μ m in F.

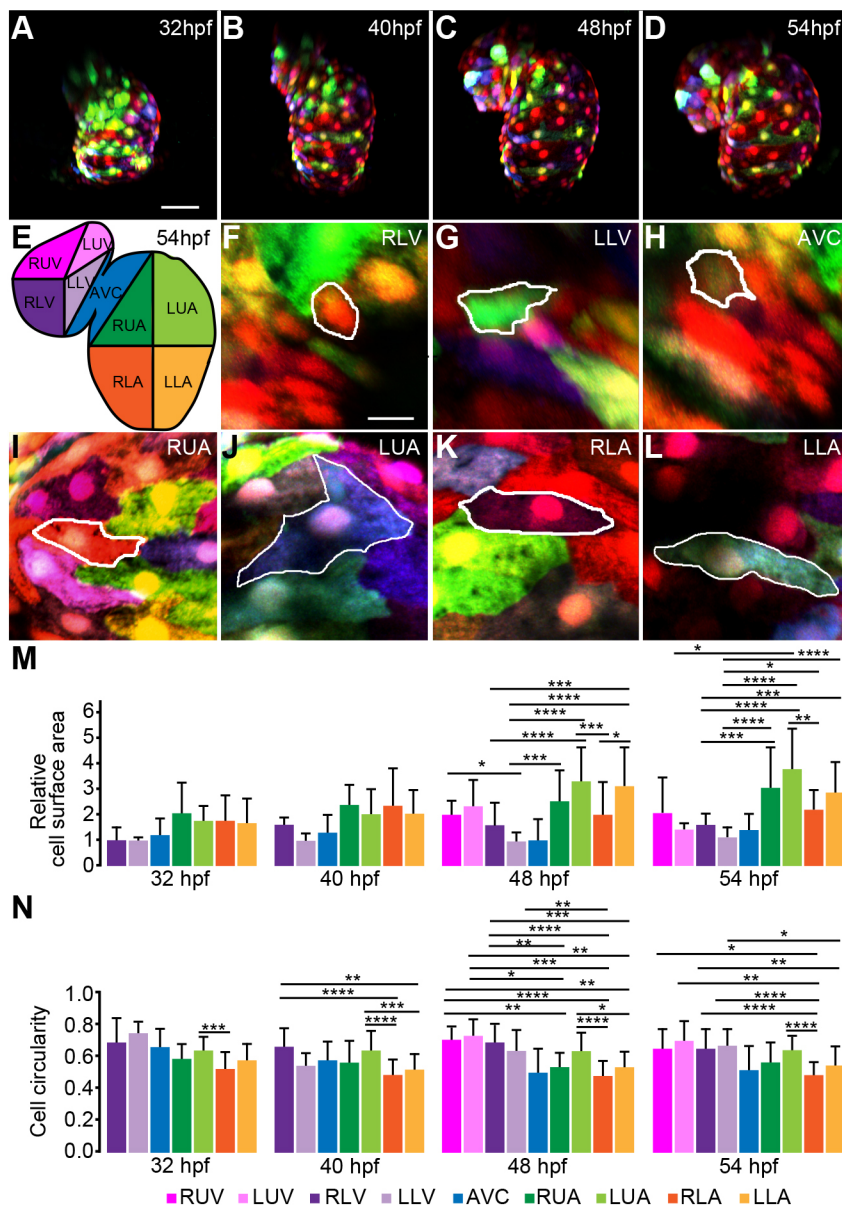
Finally, we compared the angular shifts between individual section planes to determine whether a torsional winding had occurred within the heart tube. Between 40 and 48 hpf, the angular shifts within all section planes were less than $\pm 10^\circ$, indicating only minor torsional shifts within the heart at the beginning of advanced S-looping phase [Fig. 1M; mean \pm s.d., sample size (Table S2A) and statistical analysis (Table S2B)]. However, at the end of advanced S-looping phase between 48 and 54 hpf, a strong rightward shift relative to the rest of the heart tube of -34.7° and -51° occurred mainly in the ventricular region close to the outflow tract (planes 5 and 6, respectively)

(Fig. 1N,P, red arrows; Table S2A,B). In comparison, section planes at the lower atrium (planes 1, 2) had only a minor leftward torsional movement, with positive angular shifts of $+3.5^\circ$ and $+8.8^\circ$, respectively. Similarly, section planes closest to the AVC (planes 3, 4) had only low negative angular shifts of -4.6° and -1.5° , respectively. Fig. 1O shows the angular shifts between 40 and 54 hpf (Fig. 1O; Table S2A,B). Hence, between 48 and 54 hpf, zebrafish S-looping involves a torsional winding within the heart tube that is particularly strong within the region of the ventricle closest to the outflow tract.

In order to assess the impact of cellular dynamics and morphologies on S-looping morphology, we combined the multi-color mosaic-labeling approach with high-resolution live imaging at 32, 40, 48 and 54 hpf (Fig. 2A-D; Fig. S2). This approach allowed us to analyze cell morphologies and positions of individual cardiomyocytes during these cardiac looping stages. In contrast to a more conventional subdivision of the heart chambers into an inner curvature (IC) comprising the regions neighboring the AVC and an outer curvature (OC) comprising the residual regions of atrium and ventricle, we used a more-detailed subdivision of the heart to characterize regional myocardial cell morphologies (Fig. 2E). Accordingly, heart chambers were subdivided along their R-L and cranial-caudal axes, which resulted in nine regions (Fig. 2E-L). To assess cell morphology changes, myocardial cell surface area and circularity were quantified using Fiji software. An extensive comparison of these morphological parameters revealed highly dynamic changes of cell morphologies with regional characteristics during cardiac looping morphogenesis (Fig. 2M,N; statistical

analysis in Tables S3 and S4, respectively). Ventricular cardiomyocytes were generally smaller and more circular, with fewer regional differences than atrial cardiomyocytes. In general, regional differences, both between chambers and within the atrium, were more significant from 48 hpf. At 48 and 54 hpf, cells located on the left side of the atrium (LLA+LUA) were larger and more circular than cells located within the corresponding right atrial regions (RLA+RUA). Myocardial cells close to the inflow tract (regions RLA+LLA) acquired highly elongated shapes, whereas cells in the left upper atrium (LUA) acquired large and rounded shapes. These dynamic regional morphologies correspond with regionally anisotropic ballooning of the heart chambers, which contributes to the S-looped heart morphology.

Taken together, S-looping morphogenesis in zebrafish coincides with planar bending of the heart tube, a torsional deformation that is particularly strong within the proximal part of the ventricle, and an anisotropic ballooning of the heart chambers corresponding with regionally confined changes in cardiomyocyte morphology.



Bmp signaling activity is asymmetric during S-looping morphogenesis

To elucidate molecular regulatory mechanisms that control cardiac S-looping, we first focused on the role of Bmp signaling due to its well-established role in controlling cell morphological changes that contribute to organ morphogenesis (Jidigam et al., 2015; Widmann and Dahmann, 2009). First, we analyzed the spatial-temporal activity of Bmp signaling within hearts between 24 and 54 hpf using the transgenic *Tg(BRE-AAVmlp:dmKO2)^{mw40}* Bmp reporter line (Collery and Link, 2011) [referred to as *Tg(BRE:dmKO2)^{mw40}*]. This reporter expresses destabilized monomeric Kusabira-Orange 2

(dmKO2) under the control of a Bmp-responsive element (BRE), which contains multiple binding sites for phosphorylated Smad (P-Smad) proteins. A C-terminal PEST domain mediates rapid degradation of dmKO2, which enables a precise monitoring of Smad-dependent Bmp pathway activity. For a time course analysis of Bmp signaling activity during cardiac looping stages, we imaged double-transgenic *Tg(BRE:dmKO2)^{mw40}* (false-colored gray) and *Tg(kdr1:EGFP)^{s843}* (false-colored red) hearts at 24, 30, 36, 42, 48 and 54 hpf (Fig. 3A-F; Fig. S3). At early heart stages (24 and 30 hpf), Bmp signaling activity was higher in endocardium compared with myocardium (Fig. 3A,B; Fig. S3A-B

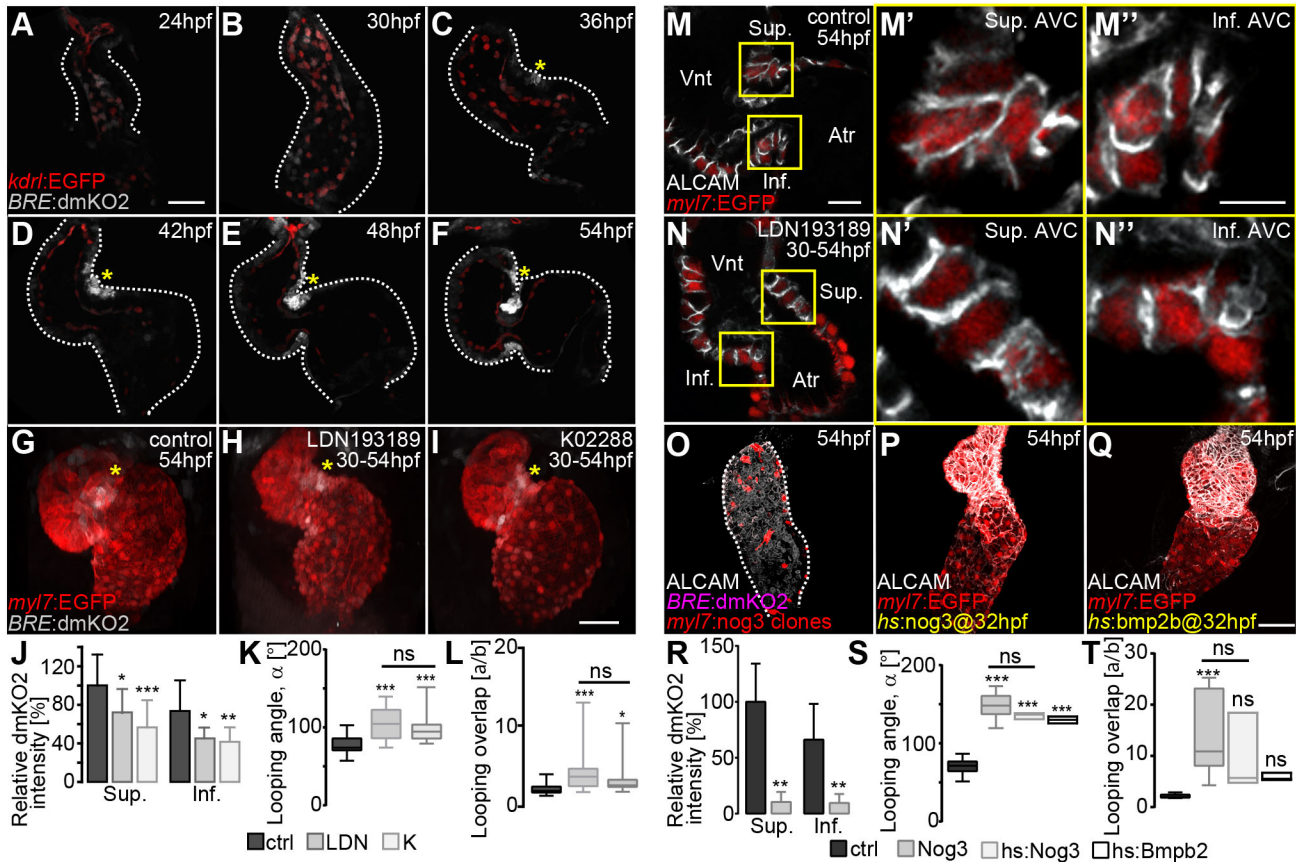


Fig. 3. Bmp signaling activity is asymmetric during S-looping morphogenesis. (A-F) Reconstructions of confocal z-scans of wild-type hearts expressing the Bmp signaling reporter transgene *Tg(BRE:dmKO2)^{mw40}* (false-colored gray) in combination with the *Tg(kdr1:EGFP)^{s843}* endocardial/endothelial reporter line (false-colored red) during heart looping morphogenesis (myocardium, dotted lines). (A,B) Initially, Bmp signaling is present within the entire endocardium and only weakly expressed within the myocardium. During early (C,D) and advanced (E,F) S-looping stages, BMP activity increases at the superior AVC (yellow asterisks) and more weakly at the inferior AVC. (G-L) Pharmacological inhibition of Bmp signaling using LDN193189 (20 μ M) and K02288 (20 μ M) inhibitors between 30 and 54 hpf. (G-L) Reconstruction of confocal z-stacks of the Bmp *Tg(BRE:dmKO2)^{mw40}* and myocardial *Tg(myI7:EGFP)^{mw34}* (false-colored red) reporter lines treated with (G) 0.2% DMSO (control), (H) LDN193189 or (I) K02288. Both LDN193189 and K02288 result in defective cardiac looping. Yellow asterisks highlight Bmp signaling within myocardium. (J-L) Bmp inhibition decreases the relative dmKO2 intensity at the superior (Sup.) and inferior (Inf.) AVC (J), increases the looping angle (α) (K) and decreases the looping overlap (increase in the index a/b) (L). (M-N^{''}) Myocardial cell morphologies within the superior and inferior AVC after Bmp inhibition. (M,N) Single z-stack section images of ALCAM immunolabeled (false-colored white) and *Tg(myI7:EGFP)^{mw34}* myocardial reporter-expressing hearts (false-colored red) of embryos treated (M) with 0.2% DMSO (control) or (N) with LDN193189 between 30 and 54 hpf. (M^{''}-N^{''}) Enlargements of the areas outlined in M and N. Whereas myocardial cells at the superior AVC of control hearts have a columnar and conical shape (M^{''}), the morphologies of AVC cells are cuboidal after Bmp inhibition (N^{''}). Myocardial cells at the inferior AVC are cuboidal in control (M^{''}) and in LDN-treated (N^{''}) hearts. (O-T) Alterations in BMP signaling affect cardiac S-looping. (O-Q) Reconstructions of confocal z-scans of representative hearts. (O) Clonal overexpression of the BMP antagonist Noggin 3 causes a downregulation of the Bmp reporter transgene *Tg(BRE:dmKO2)^{mw40}* within the heart and an abnormal morphology. Overexpression of either (P) Noggin 3 [*Tg(hsp70l:Nog3)^{fr14}* transgenic line] or (Q) Bmp2B [*Tg(hsp70l:Bmp2b)^{fr13}* transgenic line] by heat shock at 32 hpf causes cardiac looping defects at 54 hpf. (R) Clonal overexpression of Noggin 3 decreases expression of the Bmp reporter transgene *Tg(BRE:dmKO2)^{mw40}* at the superior (Sup.) and inferior (Inf.) AVC (Table S5). (S,T) Misregulated Bmp signaling causes an increase in looping angles (α) (Table S1) (S) and in the index a/b (Table S1) (T). In K,L,S,T, the limits of the boxes indicate the range between the first quartile (25th percentile) and the third quartile (75th percentile). The line inside box indicate the median value. The error bars indicate the maximum and minimum values. Data are mean \pm s.d. in J,R; ns, not significant; * $P\leq 0.05$; ** $P\leq 0.01$; *** $P\leq 0.001$. Scale bars: 50 μ m in A-I,O-Q; 20 μ m in M,N; 10 μ m in M^{''}-N^{''}.

"), which is consistent with its role in endocardial cell proliferation (Dietrich et al., 2014). Within myocardial tissue, the Bmp reporter activity became apparent at the future superior AVC region of the early S-looped 36 hpf heart, immediately prior to the onset of the advanced S-looping phase (Fig. 3C, asterisk; Fig. S3C-C"). Throughout cardiac looping stages (36-54 hpf), Bmp activity was more pronounced within the superior compared with the inferior AVC, which created an asymmetric pattern of activity (Fig. 3C-F, asterisks; Fig. S3C-F"). These observations raised the intriguing possibility that asymmetric Bmp activity might play a role in the regulation of zebrafish S-looping. The asymmetry of Bmp signaling activity within the superior AVC myocardial tissue was verified by immunolabeling against P-Smad1/5/8 (Fig. S4A,C). However, with respect to its onset, an asymmetric P-Smad1/5/8 immunostaining at the future superior AVC region within myocardial tissue was observed as early as at the linear heart tube stage (30 hpf) (Fig. S4A), which preceded the asymmetric expression of the Bmp reporter line by 6 h (Fig. 3C). To evaluate the specificity of Bmp signaling activity indicated by the P-Smad1/5/8 immunostaining, we carried out pharmacological inhibition with 20 μ M LDN193189 treatment between 24 and 30 hpf (Fig. S4B) and 24 and 54 hpf (Fig. S4D), and found that the immunostaining signal strongly decreased compared with the 0.2% DMSO-treated control hearts (Fig. S4A,C). Hence, BMP signaling activity is stronger at the superior compared with the inferior AVC during S-looping stages.

To further analyze the involvement of Bmp signaling in heart looping, we used the two specific small molecule inhibitors [LDN193189 (Cuny et al., 2008; Dietrich et al., 2014) and K02288 (Sanvitale et al., 2013)] between 30 and 54 hpf (Fig. 3G-I). Both compounds interfere with Bmp signaling by preventing the activation of the Smad-dependent pathway via Bmp type I receptors. Indeed, both inhibitors caused a significant reduction of the relative dmKO2 fluorescence intensity levels within the superior or inferior myocardial AVC when compared with DMSO-treated control hearts (superior AVC: control, 100 \pm 32%; LDN193189, 71 \pm 25%; K02288, 57 \pm 28%; inferior AVC: control, 74 \pm 32%; LDN193189, 45 \pm 11%; K02288, 42 \pm 15%) (Fig. 3J; sample size and statistical analysis in Table S5). Next, we assessed the extent of S-looping after Bmp signaling inhibition by quantifying the looping angle (α) (LDN193189, 105 \pm 20 $^\circ$; K02288, 98 \pm 16 $^\circ$) and index a/b (LDN193189, 4.3 \pm 2.6; K02288, 3.3 \pm 1.7) compared with control hearts (control, 77 \pm 12 $^\circ$; control, 2.2 \pm 0.7, respectively) (Fig. 3K,L; sample size and statistical analysis in Table S1). In comparison with DMSO-treated control hearts, the looping angles in LDN193189- or K02288-treated hearts were significantly higher, which shows that these Bmp signaling-inhibited hearts were more linear (Fig. 3H,I,K; Table S1; Fig. S4D). Consistent with this finding, the index a/b was significantly increased in LDN193189- or K02288-treated hearts, which also implies a reduced lateral overlap of the heart chambers and thus a more linear heart morphology (Fig. 3H,I,L; Table S1; Fig. S4D). Thus, abnormal S-looping may be affected by abnormal planar bending.

The essential role of Bmp in this morphogenetic process was demonstrated by higher Bmp reporter signaling at the superior AVC myocardium that coincided with the onset of S-looping and by a failure of correct S-looping upon pharmacological Bmp signaling inhibition. This also suggested an involvement of Bmp activity in planar bending of the heart tube, as indicated by the more linear morphology of Bmp signaling-inhibited hearts. To analyze whether Bmp promotes planar bending by driving cell morphology changes, we used an antibody against the cell-adhesion protein ALCAM to

outline cell borders and closely examined the cellular morphologies of superior and inferior AVC myocardial cells in control embryos and in embryos treated with LDN193189 (Fig. 3M-N"). Single confocal z-scan images at the AVC revealed that 54 hpf myocardial cells at the superior AVC have a conical shape and are 'bottlenecking' (Fig. 3M,M'), which may contribute to the constriction of the AVC and facilitate bending of the heart tube. In contrast, hearts treated with 20 μ M LDN193189 between 30 and 54 hpf had more cuboidal shapes (Fig. 3N,N'), which is similar to myocardial cell shapes present at earlier stages (Fig. S5A,A'). At 54 hpf, myocardial cells at the inferior AVC had cuboidal shapes in both control (Fig. 3M,M") and LDN193189-treated hearts (Fig. 3N,N"). Hence, Bmp inhibition caused reduced bending of the heart and resulted in more cuboidal myocardial cell morphologies at the superior AVC that resemble those cell morphologies present at the onset of S-looping when the Bmp signaling asymmetry initiates at the superior AVC.

In a complementary approach, we assayed whether misregulation of Bmp signaling during S-looping morphogenesis causes any planar-bending defects (Fig. 3O-T). To downregulate Bmp signaling, we clonally overexpressed the secreted Bmp antagonist Noggin3 within myocardial tissue (Fig. 3O) or overexpressed Noggin3 from the stable *Tg(hsp70l:Nog3)^{fr14}* (Chocron et al., 2007) transgenic line of zebrafish by heat shock at 32 hpf (Fig. 3P). We found that these conditions had a stronger effect on planar bending compared with the pharmacological inhibition of BMP signaling. The stronger effect of Noggin3 clonal overexpression (Fig. 3O) in comparison with pharmacological (Fig. 3H,I) or genetic (Fig. 3P) inhibition of BMP signaling could be due to the fact that myocardial clones are expressing Noggin3 from the onset of cardiac morphogenesis. Instead, the timing of the Bmp inhibition treatment between 30 and 54 hpf, and of the heat shock at 32 hpf, may have had less of an impact on the process of cardiac looping. Overexpression of the Bmp2b ligand was induced from the stable heat-shock promoter-driven transgene *Tg(hsp70:Bmp2b)^{fr13}* (Chocron et al., 2007) at 32 hpf (Fig. 3Q). In all cases, hearts analyzed at 54 hpf were abnormally looped (Fig. 3O-Q), as quantified by S-looping parameters (Fig. 3S,T). For clonally overexpressed Noggin3, it was also possible to measure the relative dmKO2 fluorescence intensities showing that Bmp signaling was reduced at both superior and inferior AVCs (Fig. 3R; sample size and statistical analysis in Table S5) (superior AVC: control, 100 \pm 34%; Nog3 clonal overexpression, 10 \pm 9%; inferior AVC: control, 66 \pm 32%; Nog3 clonal overexpression, 10 \pm 8%). Looping angles increased in all three conditions (Nog3 clonal overexpression, 149 \pm 8 $^\circ$; hs:Noggin3, 137 \pm 4 $^\circ$; hs:Bmp2b, 130 \pm 4 $^\circ$) in comparison with control hearts (73 \pm 10 $^\circ$) (Fig. 3S; sample size and statistical analysis in Table S1). The index a/b increased in all conditions when compared with control hearts, which also suggested defective bending and a more linear heart upon loss of Bmp signaling (Nog3 clonal overexpression, 14 \pm 8; hs:Noggin3, 9 \pm 8; hs:Bmp2b, 5.9 \pm 0.8; control, 1.9 \pm 0.4) (Fig. 3T; sample size and statistical analysis in Table S1). A closer examination of the AVC regions revealed that these cardiomyocytes had abnormal cell shapes under conditions of downregulation or overactivation of Bmp signaling (Fig. S5B-C"). Hence, the reduction in chamber overlap, and thus in S-looping, when Bmp signaling is misregulated suggested that fine-tuning of the Bmp signaling pathway is needed for ensuring normal planar bending of the heart during S-looping morphogenesis. Indeed, Bmp modulates this process apparently by regulating the acquisition of conical and bottlenecked cell shapes of myocardial cells within the superior AVC region.

Establishment of asymmetric Bmp signaling within the AVC is not dependent on Nodal or Wnt signaling

Cardiac looping morphogenesis can occur in zebrafish embryos with defective L/R asymmetry (Burdine and Schier, 2000). This raises the issue of whether and how asymmetric Bmp signaling at the AVC is initially established. We therefore analyzed developmental pathways that determine the general body plan of the embryo, including Nodal and Wnt signaling. First, we downregulated Nodal signaling by injection of an antisense oligonucleotide morpholino (MO) against the primary cardiac Nodal ligand Southpaw (Spaw), which is a key regulator of cardiac L/R asymmetry (Long et al., 2003; Rebagliati et al., 1998; Smith et al., 2011; Veerkamp et al., 2013). Knockdown of Nodal signaling caused a randomized looping of the heart in the right-left (R-L) embryonic body axis with D-looped (54%) (Fig. 4A) and L-looped (27%) (Fig. 4B) hearts, and an abnormal looping along the dorsal-ventral (D-V) embryonic body axis with V-looped (19%) hearts (Fig. 4C) ($n=83$ embryos). Bmp signaling activity was in an asymmetric pattern that strictly correlated with the orientation of S-looping (Fig. 4D,E) when hearts were looping along the R-L axis (D- and L-looped hearts). Despite a lack of Nodal signaling, these hearts looped to a degree comparable with wild type (D-looped heart, 2.3 ± 0.4 ; L-looped heart, 2.4 ± 0.4) (Fig. 4G; Table S1). For the third group of hearts that were looping within the D-V axis (Fig. 4C,F), Bmp activity was present either on both sides of the midline or with an D/V asymmetry (Fig. 4F,G; Table S1; V-looped heart index a/b , 5.4 ± 0.7). Taken together, the asymmetric expression of Bmp within the embryonic heart is independent of Nodal activity and strictly correlates with the looping orientation of D- and L-looped hearts.

To downregulate the Wnt signaling pathway, which is essential for the establishment of the embryonic cranial-caudal body axis (Yamaguchi, 2001), embryos were treated between 30 and 54 hpf with $10\ \mu\text{M}$ of the Wnt antagonist IWR-1, which stabilizes Axin1 (thereby promoting the degradation of β -catenin and inhibiting the activation of Wnt target genes) (Nusse, 2005) (Fig. 4H-L). As a proof of efficacy, during cardiac valve leaflet formation at 72 hpf, $10\ \mu\text{M}$ IWR-1 was sufficient to inhibit Wnt signaling, which was observed in transgenic embryos of the Wnt reporter line *Tg(7xTCF-Xla.Siam.nls mCherry)^{ia5}* (data not shown). Subsequently, the cardiac *Tg(BRE:dmKO2)^{mw40}* Bmp signaling reporter activity was quantified at 54 hpf (Fig. 4L). Upon Wnt signaling inhibition, cardiac S-looping at 54 hpf was not affected (Fig. 4I-K). Quantifications of planar bending in IWR-1-treated hearts based on the looping angle (α) or the index a/b did not reveal significant differences in comparison with DMSO-treated controls (Fig. 4J,K; mean \pm s.d., sample size and statistical analysis in Table S1). In addition, upon IWR-1 treatment, Bmp signaling based on dmKO2 fluorescence intensity levels showed no significant changes within superior AVC myocardial cells and only a slight reduction within inferior AVC myocardium ($P\leq 0.05$) (Fig. 4L; mean \pm s.d., sample size and statistical analysis in Table S5). Altogether, we conclude that downregulation of Wnt signaling by IWR-1 treatment from 30–54 hpf did not affect S-looping morphogenesis or the asymmetry of Bmp signaling activation within the superior AVC.

Establishment of asymmetric Bmp signaling within the AVC is dependent on cardiac contractility

Because the onset of a heart beat and blood flow coincides with the initial stages of cardiac looping, we next analyzed whether changes in hemodynamic forces or cardiac contractility affect cardiac looping. Both Gata1 and Gata2 are transcription factors required

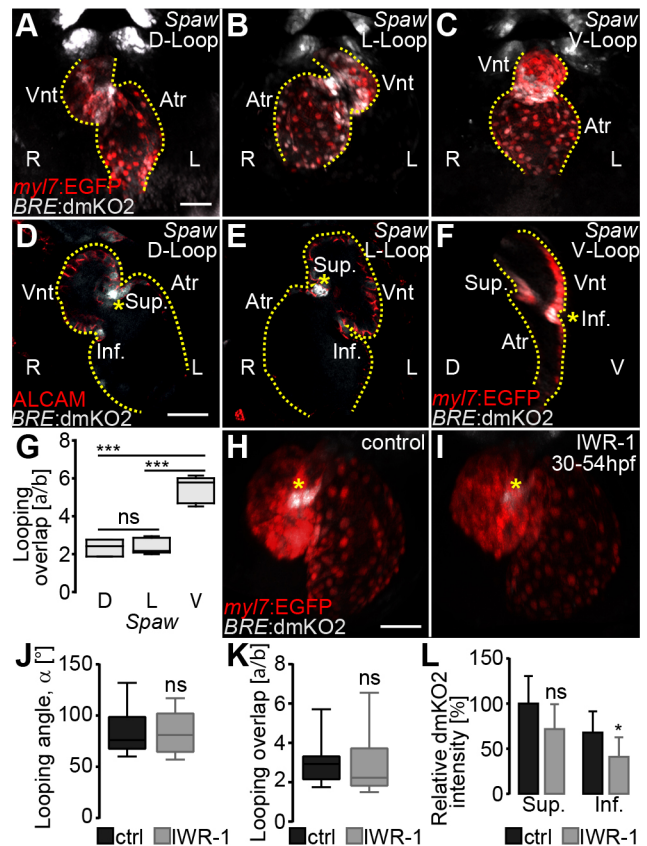


Fig. 4. Establishment of asymmetric Bmp signaling within the AVC is not dependent on Nodal or Wnt signaling. (A–C) Loss of the Nodal ligand Spaw results in D-looped (A), L-looped (B) or V-looped (C) hearts (D, L and V refer to the ventricular position with respect to embryonic body axes).

(A–C) Reconstructions of confocal z-scans of representative 54 hpf *spaw* morphant hearts with expression of Bmp *Tg(BRE:dmKO2)^{mw40}* (false-colored gray) and myocardial *Tg(mly7:EGFP)^{twu34}* (false-colored red) reporter lines. Frontal view of hearts imaged on fixed embryos. R, right; L, left embryonic side. (D,E) Confocal z-stacks in the right-left (R-L) plane of representative D- (D) and L- (E) looped hearts with Bmp signaling activity, as indicated by *Tg(BRE:dmKO2)^{mw40}* and myocardial cell borders immunolabeled against ALCAM (false-colored red). Hearts looped within the R-L plane show Bmp activity in both chirality orientations within myocardial cells of the AVC (yellow asterisk). (F) Confocal z-stack image in the dorsal-ventral (D-V) plane of a V-looped heart with Bmp *Tg(BRE:dmKO2)^{mw40}* and myocardial *Tg(mly7:EGFP)^{twu34}* reporter lines. The outline of the heart is delineated by a yellow dotted line. Atr, atrium; Vnt, ventricle; Sup., superior AVC; Inf., inferior AVC. (G) Quantification of index a/b (data in Table S1). (H–L) The Wnt signaling pathway is not involved in cardiac S-looping morphogenesis. (H,I) Reconstruction of confocal z-stacks of representative transgenic hearts with the Bmp reporter *Tg(BRE:dmKO2)^{mw40}* and myocardial reporter *Tg(mly7:EGFP)^{twu34}*. 0.1% DMSO-treated (control) (H) or Wnt inhibitor IWR-1-treated (I) hearts show Bmp signaling within the myocardium (yellow asterisks). (J–L) Looping angle (α) (data in Table S1) (J), index a/b (data in Table S1) (K) and relative dmKO2 intensity (L) at the superior AVC are not significantly affected by IWR-1 treatment (data in Table S5). (L) The relative dmKO2 intensity at the inferior AVC is slightly reduced ($P\leq 0.05$) after IWR-1 treatment (statistical analysis in Table S5). In G,J,K, the limits of the boxes indicate the range between the first quartile (25th percentile) and the third quartile (75th percentile). The line inside box indicate the median value. The error bars indicate the maximum and minimum values. Data are mean \pm s.d. in L; ns, not significant; * $P\leq 0.05$, *** $P\leq 0.001$. Scale bars: 50 μm .

for hematopoiesis in zebrafish and their knockdown results in abnormal hemodynamic forces (Galloway et al., 2005). Knockdown of Gata1 shifts erythropoiesis towards myelopoiesis (Galloway

et al., 2005), which results in a complete absence of red blood cells (Lyons et al., 2002; Vermot et al., 2009) and reduces blood viscosity by 90% (Vermot et al., 2009). Loss of *Gata2* causes a reduction in blood cell numbers (Dietrich et al., 2014; Galloway et al., 2005; Tsai and Orkin, 1997; Vermot et al., 2009). As a consequence, blood viscosity in zebrafish embryos is reduced by 70% and the retrograde flow fraction is strongly reduced (Vermot et al., 2009). Combined loss of *Gata1* and *Gata2* causes a complete loss of red blood cells but a milder reduction of the retrograde flow fraction when compared with *gata2* morphants (Dietrich et al., 2014; Vermot et al., 2009). Cardiac TroponinT2a (*Tnnt2a*) is essential for sarcomere assembly and cardiac contractility (Huang et al., 2009; Sehnert et al., 2002). To assess the impact of reduced shear stress and retrograde flow fraction, or of cardiac contractility, on cardiac S-looping and on the asymmetric activation of Bmp signaling within the superior AVC, we carried out individual or combined injections of MOs against *Gata1*, *Gata2*, *Gata1/2* or *Tnnt2a* (Fig. 5A-E'). Quantification of the relative dmKO2 intensity at 54 hpf within both superior and inferior AVC myocardium revealed significant differences in Bmp reporter activity only for the condition with a lack of *Tnnt2a* (Fig. 5F; mean±s.d., sample size and statistical analysis in Table S5; superior AVC: control, 100±30%; MO *Gata1*, 59±27%; MO *Gata2*, 79±21%; MO *Gata1/2*, 60±7%, MO *Tnnt2a*, 47±12%; inferior AVC: control, 56±4%; MO *Gata1*, 31±13%; MO *Gata2*, 39±11%; MO *Gata1/2*, 34±7%; MO *Tnnt2a*, 42±14%). Hence, Bmp asymmetric activity within the AVC is significantly reduced in the absence of heart contractility and not simply by a reduction of shear stress or retrograde flow patterns. Quantification of cardiac S-looping parameters, revealed a

significant increase of the looping angle (α) (Fig. 5G; sample size and statistical analysis in Table S1; control, 82±5°; MO *Gata1*, 95±10°; MO *Gata2*, 103±13°; MO *Gata1/2*, 112±19°; MO *Tnnt2a*, 135±24°) and of the index a/b (Fig. 5H; sample size analyzed and statistical analysis are in Table S1; control, 2.1±0.2; MO *Gata1*, 3.1±0.3; MO *Gata2*, 3.4±0.7; MO *Gata1/2*, 4.6±1.6; MO *Tnnt2a*, 8.0±4.2) under conditions of loss of *Gata1/2* or *Tnnt2a*. This also correlated with changes in S-looping morphology (Fig. 5D,E). The effects of a lack of cardiac contractility were further tested in TroponinT2a (*tnnt2a*)^{b109} mutants (Sehnert et al., 2002). At 54 hpf, mutant hearts were not looped and P-Smad1/5/8 levels were reduced in myocardial AVC cells (Fig. S6B,B'). This correlated with an increase in the looping angle (α) (*tnnt2a* mutant, 125±15°; control, 93±8°) and in the index a/b (*tnnt2a* mutant, 9.6±3.5; control, 2.1±0.3) (Fig. S6D,E; sample size analyzed and statistical analysis are in Table S1). This also correlated with a loss of asymmetric BMP signaling activity within the superior AVC (Fig. S6C, sample size analyzed and statistical analysis are in Table S6). In summary, alterations of retrograde flow patterns result in S-looping defects that are not caused by obvious changes in Bmp signaling at the AVC. However, as BMP is only weakly and homogeneously active in *tnnt2a* morphant and mutant hearts, cardiac contractility is apparently an important modifier of its activity.

DISCUSSION

As discussed by Männer (2000, 2009) and Le Garrec and colleagues (2017), the definition of cardiac looping has differed in a number of studies (Le Garrec et al., 2017; Männer, 2000; Männer, 2009).

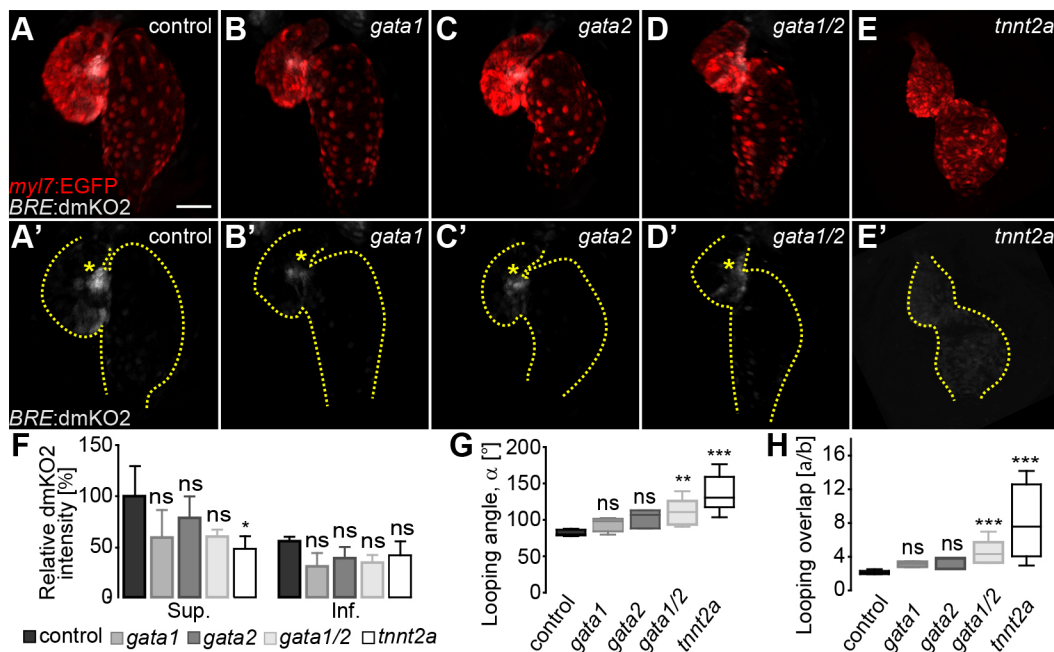


Fig. 5. Cardiac contractility is required for Bmp signaling at the superior AVC. (A-E) Reconstructions of confocal z-stacks of hearts at 54 hpf in (A) wild-type, (B) *gata1* morphant, (C) *gata2* morphant, (D) *gata1/2* double morphant or (E) *tnnt2a* morphant embryos. Myocardial tissue is marked by expression from the *Tg(mly7:EGFP)^{twu34}* reporter (false-colored red) and Bmp reporter *Tg(BRE:dmKO2)^{mw40}* (false-colored gray). (A'-E') Bmp reporter *Tg(BRE:dmKO2)^{mw40}* expression. The outline of the heart is delineated by dotted lines. Asymmetric Bmp signaling activity within the superior AVC is marked by yellow asterisks. (F-H) Quantifications of (F) relative dmKO2 intensities at the superior (Sup.) and inferior (Inf.) AVC (data in Table S5), (G) looping angle (α) (data in Table S1), and (H) index a/b (data in Table S1) were measured in *gata1*, *gata2*, *gata1/2* and *tnnt2a* morphant versus wild-type hearts. Under abnormal hemodynamic conditions (*gata1*, *gata2* and *gata1/2* morphant hearts) the relative dmKO2 intensity is not significantly affected. However, asymmetric Bmp signaling activity is lost in the absence of cardiac contractility. The looping angle (α) (G) and the index a/b (H) are significantly increased in *gata1/2* and *tnnt2a* morphant versus control hearts (statistical analysis in Table S1). In G,H, the limits of the boxes indicate the range between the first quartile (25th percentile) and the third quartile (75th percentile). The line inside box indicate the median value. The error bars indicate the maximum and minimum values. Data are mean±s.d. in F; ns, not significant; * $P \leq 0.05$; ** $P \leq 0.01$; *** $P \leq 0.001$. Scale bar: 50 μ m.

Therefore, a clear description of the morphological changes and the cellular mechanisms that contribute to zebrafish cardiac looping was needed. Here, we have characterized S-looping morphogenesis in the zebrafish and describe three cell- or tissue-scale morphogenetic processes that all contribute to the deformation of the linear heart tube (Fig. 6): (1) zebrafish S-looping involves a torque-like winding deformation mainly at the arterial pole of the early heart tube; (2) anisotropic growth of ventricle and atrium along their outer curvatures contributes to the emergence of the S-shaped morphology of the zebrafish heart; and (3) Bmp signaling is an intrinsic signaling pathway that controls cell shape changes at the superior myocardial wall of the AVC, which determines bending of the heart tube.

Some of these cellular processes are remarkably similar to morphogenetic processes within higher vertebrates. Rotation of the outflow tract region has been observed in the chick (Thompson et al., 1987) and mouse embryo (Meilhac et al., 2004; Bajolle et al., 2006). Anisotropic growth of cardiomyocytes during cardiac looping has also been described in higher vertebrates (Kidokoro et al., 2008; Manasek et al., 1972; Meilhac et al., 2004; Shi et al., 2014a; Soufan et al., 2006; Voronov et al., 2004). In zebrafish, blood flow is an important trigger that causes the elongation of ventricular cardiomyocytes within the outer curvature. Heart contractility has some role in restricting the extent of their elongation (Auman et al., 2007). This balanced interplay between contractility as a cell-intrinsic

force and blood flow as an extrinsic force demonstrates the interdependence of these forces in shaping the developing heart (Auman et al., 2007; Deacon et al., 2010). Our data extend these previous studies and provide a dynamic multi-color mosaic labeling-based view of this process over the course of cardiac looping. This analysis also reveals that regionally confined anisotropic growth of cardiomyocytes contributes to chamber morphogenesis in a way that contributes to the cardiac S-shaped morphology.

Several lines of evidence suggest that Bmp signaling acts as an intrinsic signaling pathway during cardiac S-looping morphogenesis. Unlike Nodal, which is not expressed within the mouse heart tube at looping stages (Vincent et al., 2004), we find that, in zebrafish, Bmp signaling has an asymmetric activity within the heart that strongly correlates with looping orientation and is not dependent on the Nodal ligand Spaw. Similar patterns of Bmp expression are also present in the hearts of higher vertebrates (Jiao et al., 2003; Somi et al., 2004) and *bmp4* is asymmetrically expressed within the zebrafish heart at the cone stage prior to the formation of a heart tube (Chen et al., 1997; Smith et al., 2008; Somi et al., 2004; Veerkamp et al., 2013). However, to date the role of Bmps in cardiac looping morphogenesis beyond their well-established role in L/R asymmetry within the embryo (Breckenridge et al., 2001; Chen et al., 1997; Chocron et al., 2007; Ocaña et al., 2017; Smith et al., 2008; Veerkamp et al., 2013; Zhang and Bradley, 1996) and in the formation of the AVC region

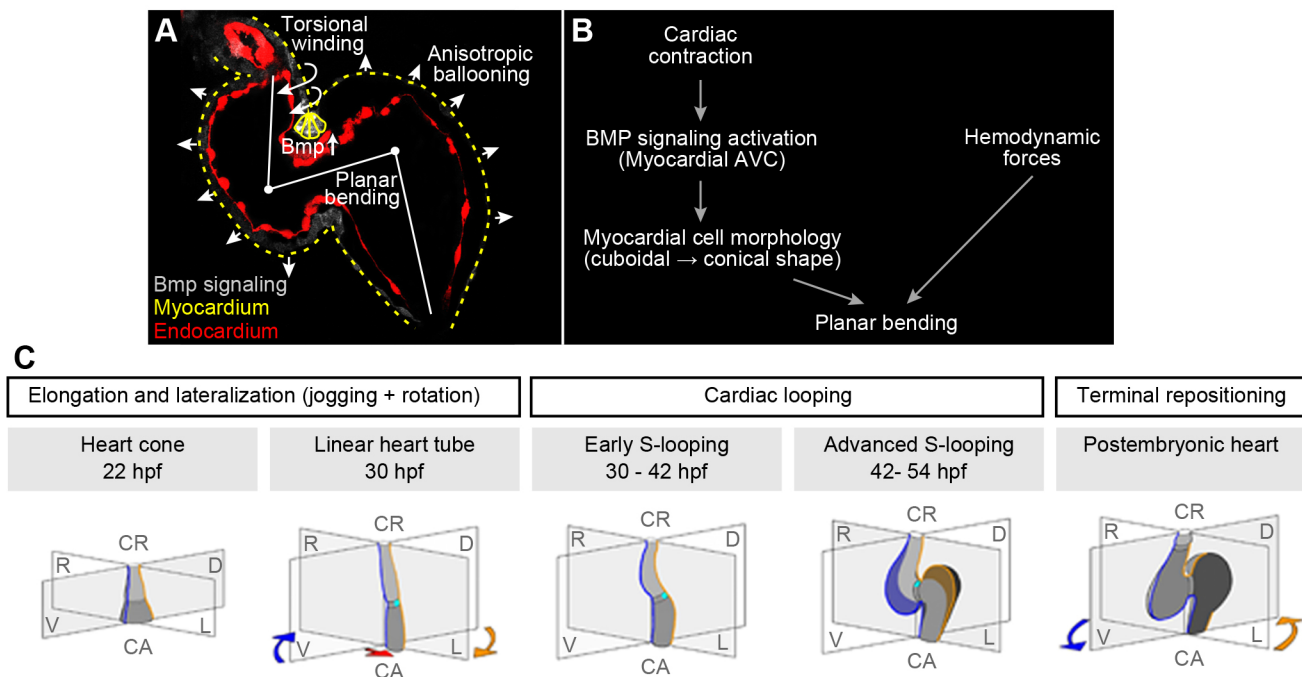


Fig. 6. Model of zebrafish cardiac looping. (A) Summary of cellular processes that contribute to zebrafish S-looping morphogenesis: (1) BMP-dependent planar bending (white line at heart midline) of the heart tube due to cuboidal-to-conical cell shape changes of superior AVC cardiomyocytes (yellow triangles); (2) myocardial anisotropic ballooning due to region-specific cell morphology changes causes an expansion of the two cardiac chambers (white arrowheads); and (3) ventricular rightward-torsional winding (twisted arrows at ventricular outflow tract) is most pronounced at the cranial pole of the heart. Bmp signaling (false-colored gray) with strong activation at myocardial superior AVC, myocardium (yellow dotted lines) and endocardium (false-colored red). (B) Summary of cell-intrinsic and -extrinsic factors involved in cardiac planar bending of the heart tube. Cardiac contractility is essential for a strong Bmp signaling pathway activation within myocardial cells at the superior AVC region. This Bmp activation induces myocardial changes from cubical to conical cell shapes and results in an S-planar bending of the heart tube. In addition, hemodynamic forces (shear stress and retrograde flow fraction) affect Bmp signaling-independent planar bending. (C) During zebrafish cardiac looping morphogenesis, two separate processes occur in parallel: (1) planar S-looping along the mid-sagittal body axis and (2) lateral looping during which the ventricle is positioned towards the right and the atrium towards the left (D-looping). The mid-sagittal plane is in grey; original right and left sides of the heart are marked in blue and yellow, respectively. Under some experimental conditions, inverted L-looping can also occur. In comparison with lung-breathing vertebrates, the zebrafish atrium turns around the cardiac cranio-caudal axis. The rotation of the atrium turns the cross-section plane of the AVC along the cranio-caudal axis towards the right. This movement is 'corrected' during repositioning, which places the ventricle and atrium into an almost bilateral symmetrical position again.

(Ma et al., 2005; Yamada et al., 2000) have not been addressed. A reduction of blood flow in *gata1/2* single and double morphants does not reduce Bmp activity, which correlates asymmetrically with the orientation of cardiac looping, but when cardiac contractility is also inhibited, Bmp signaling is reduced and homogeneously present within the myocardium. It remains to be elucidated in more detail whether and how mechanosensitive cardiac signaling (Paolini and Abdelilah-Seyfried, 2018) impinges upon Bmp signaling. Taken together, cell-intrinsic contractility of cardiomyocytes is apparently required as a cue for asymmetric Bmp signaling activity within the heart. In turn, Bmp signaling impacts cell shape changes of AVC myocardial cells. It has already been suggested that these morphological cell shape changes promote the constriction of the AVC (Chi et al., 2008). Concomitantly, the expression of *bmp4* becomes restricted mainly to the AVC myocardium and the outflow tract (Walsh and Stainier, 2001). A similar role has been attributed to *bmp2* during the looping morphogenesis of the avian small intestine (Fig. 6) (Nerurkar et al., 2017).

Bmp signaling is an important regulator of actomyosin contractile networks that are a driving force for cell shape changes. Signaling via the *Drosophila* Bmp ortholog Dpp controls the subcellular distribution of the small GTPase Rho1 and regulatory light chain of non-muscle myosin II, which results in an elongation of wing epithelial cells along their apical-basal axis (Widmann and Dahmann, 2009). In chick, Bmp-mediated apical accumulation of F-actin and non-muscle myosin II is involved in apical constriction prior to the invagination of epithelial sheets during sensory placode formation (Jidigam et al., 2015; Rajagopal et al., 2009). During early zebrafish cardiogenesis, Bmp induces the expression of actomyosin network components, thereby affecting both cell shapes and epithelial states of cardiac progenitor cells (Veerkamp et al., 2013). Strikingly, at cardiac looping stages, actomyosin-based contractility is most pronounced in apical membranes of outflow tract cells and this tissue polarization is required for cardiac looping (Merks et al., 2018). Currently, a potential role of BMP signaling in regulating cell shape changes during cardiac looping morphogenesis has not been explored.

Experimental studies have revealed that isolated heart tubes from amphibian, avian and zebrafish embryos can undergo ventricular bending in *in vitro* cultures due to an intrinsic capacity for this process (Bacon, 1945; Butler, 1952; Ekman, 1925; Manning and McLachlan, 1990; Noël et al., 2013). This may be due to anisotropic changes in cell shapes or sizes within the myocardial wall of the heart tube (Shi et al., 2014b; Taber, 2006). Our results are in tune with this concept and suggest that intrinsic bending mechanisms may be conserved across vertebrate species. However, not only intrinsic but also extrinsic bending mechanisms are conserved in vertebrates. Recent data from *in vivo* experiments in several model organisms (zebrafish, *Xenopus laevis*, chick, mice) strongly suggest that growth defects of the heart tube and/or pericardial cavity also play fundamental roles in the pathogenesis of anomalies in cardiac looping (reviewed by Bayraktar and Männer, 2014). The elongation of the looping heart tube is mainly driven by the addition of primary extracardiac cells to the venous and arterial heart poles (Kelly et al., 2014; Zhou et al., 2011). When the numbers of cardiomyocytes added to the heart poles during looping morphogenesis were experimentally increased or reduced, heart tubes became hyperlooped or incompletely looped in mice (Risebro et al., 2006; Srivastava et al., 1997) or in zebrafish (Schindler et al., 2014; Zhou et al., 2011). Hence, despite some morphological differences in the looping of the zebrafish heart and the tubular heart of higher vertebrates (Fig. S7), cardiac looping morphogenesis may in

principle be driven by the same fundamental biophysical forces in lower and higher vertebrates. Thus, understanding cardiac development in zebrafish, at a cellular resolution and with high molecular precision, will also be essential for a better understanding of human congenital heart defects.

MATERIALS AND METHODS

Zebrafish lines

Zebrafish were kept according to standard laboratory procedures (Westerfield, 2007). Handling of zebrafish was carried out in compliance with German and Berlin state law, carefully monitored by the local authority for animal protection (LaGeSo, Berlin-Brandenburg, Germany and LANUV, Lower-Saxony, Germany). We used the following zebrafish mutant and transgenic lines: *tmt2a^{b109}* (Sehnert et al., 2002), Tg(*kdr1:EGFP^{s843}*) (Jin et al., 2005), Tg(*myl7:EGFP^{mw34}*) (Huang et al., 2003), Tg(*BRE-AAVmlp:dmKO2^{mw40}*) (Collery and Link, 2011), Tg(*hsp70l:Nog3^{fr14}*) (Chocron et al., 2007) and Tg(*hsp70:Bmp2b^{fr13}*) (Chocron et al., 2007).

Antisense oligonucleotide morpholinos

Knockdown studies were performed by MO injection as described previously (Nasevicius and Ekker, 2000). The following antisense oligonucleotide morpholinos (Gene Tools) were used: *gata1a_ATG* MO, 5'-CTGCAAGTG-TAGTATTGAAGATGTC-3' (Galloway et al., 2005); *gata2a_3ex/in* MO, 5'-CATCTACTACCAGTCTGCGCTTTG-3' (Galloway et al., 2005); *spaw_ATG* MO, 5'-GCACGCTATGACTGGCTGCATTGCG-3' (Long et al., 2003); and MO1-*tmt2a*, 5'-CATGTTTGTCTGATCTGACACGCA-3' (Sehnert et al., 2002).

Morpholino solution (1 nl) was injected into the yolk at the following concentrations: 1 mM MO *spaw*, 1 mM MO *gata1*, 0.2 mM MO *gata2* and 0.1 mM MO1-*tmt2a*.

Pharmacological treatments

For pharmacological treatments, embryos were incubated in egg-water supplemented with 20 μ M LDN193189 trichloride (Axon Medchem, Axon 1509), 20 μ M K02288 (Sigma-Aldrich, SML1307) or 10 μ M IWR-1 (Sigma-Aldrich, I0161). If not stated otherwise, embryos were treated between 30 and 54 hpf at 28.5°C. Control embryos were incubated in egg-water containing an equal amount of DMSO.

Gene overexpression via heat shock

For heat-shock-induced overexpression of a gene of choice, transgenic embryos carrying the respective gene under control of the heat-shock promoter *hsp70l* were transferred to a 2 ml reaction tube. Heat-shock was induced at 32 hpf by addition of pre-warmed egg-water of 38°C and incubated at 38°C with shaking at 300 rpm for 45 min. After heat-shock, embryos were transferred to petri dishes filled with egg-water and incubated at 28.5°C until 54 hpf. Efficacy of the heat-shock-induced overexpression was monitored by expression of GFP within the entire embryo.

Immunohistochemistry

Embryos of the desired developmental stage were dechorionated, anesthetized with 0.16 mg/ml tricaine and fixed in 4% paraformaldehyde overnight at 4°C. Embryos were rinsed four times with phosphate-buffered saline with Tween 20 (PBST) for 10 min and blocked for 2 h at room temperature in PBST supplemented with 10% normal goat serum (NGS). Subsequently, embryos were incubated with the primary antibody mouse anti-Alcam (1:100; Developmental Studies Hybridoma Bank, zn-8) at 4°C overnight. After washing with PBST containing 5% NGS, fluorescently conjugated secondary antibody goat anti-mouse Dylight649 (1:200; Jackson Immuno Research, 115-495-003) was incubated overnight at 4°C and washed as described before. The pSmad-1/5/8 labeling was performed as described by Lenhart et al. (2013) using the following antibodies: rabbit anti-pSmad-1/5/8 (1:100; Cell signaling Technology, 9511), chicken anti-GFP (1:600; Aves labs, GFP-1020), goat anti-rabbit Dylight 649 (1:200; Jackson Immuno Research, 111-495-003) and goat anti-chicken FITC (1:200; Aves labs, F-1005). Dissected hearts were mounted in SlowFade Gold (Invitrogen, S36936) and imaged on a Leica TCS SP8 or a Zeiss LSM

510 META NLO confocal microscope with a 40× objective. Images were analyzed using Velocity 3D Image Analysis Software (Perkin Elmer) or Imaris software (Bitplane).

Clonal overexpression and plasmid constructs

For clonal Noggin3 overexpression within myocardial cells, the Tol2 plasmid myl7:nog3-IRES:GFP was co-injected with transposase mRNA in one-cell transgenic *Tg(BRE-AAVmlp:dmKO2)^{mw40}* Bmp reporter embryos. The myl7:nog3-IRES:GFP expression vector was generated by Gateway cloning (Invitrogen, 12537-103) using the following primers for *nog3* (GenBank Accession Number AL935268): *nog3_attB1_fwd* primer, 5'-GGGGACAAGTTTGTACAAAAAAGCAGGCTTCACCATGGATAAC-ATCCCGTATTTCC-3'; and *nog3_attB2_rev* primer, 5'-GGGGACCAC-TTTGTACAAGAAAGCT-GGGTTTCAGTTCGGGCAGGAGC-3'.

Multicolor mosaic-labeling approach

To unambiguously identify cardiomyocytes, myl7:TagRFP-T and myl7:TagBFP constructs [kindly provided by D. Stainier (Staudt et al., 2014), Max Planck Institute for Heart and Lung Research, Bad Nauheim, Germany] together with transposase mRNA were co-injected into 1- to 4-cell-stage embryos of the transgenic *Tg(myl7:EGFP)^{mw34}* line. Tol2-mediated transgenesis (Kawakami, 2007) resulted in a clonal expression pattern of these constructs, creating numerous differently colored cardiomyocytes throughout the entire myocardium by random combination as well as different cytoplasmic expression levels of the three fluorescent proteins. High-resolution live imaging of each single heart was performed at regular intervals during cardiac looping development. Before imaging, each live embryo was incubated with 0.16 mg/ml tricaine (3-amino benzoic acid ethylester; Sigma-Aldrich, A-5040) and 4 mg/ml of the myosin ATPase inhibitor BDM (2,3 butanedione monoxime; Sigma-Aldrich, B0753) to anesthetize and suppress the heartbeat, and then mounted in 1% low-melting agarose (Lonza, 50081) supplemented with tricaine and BDM. To ensure physiological heart development, embryos were extracted from agarose directly after imaging and kept in egg-water at 28.5°C until the next imaging time-point. Hearts were imaged on a confocal laser scanning microscope (Leica TCS SP8) with a 20× objective. Images were analyzed using IMARIS Image Analysis Software (Bitplane).

Calculation of looping angle (α), index value (a/b) and relative dmKO2 or P-Smad1/5/8 fluorescence intensity

Looping angle (α) and index value (a/b) were calculated on the 2D heart projection of confocal z-stacks using Fiji software (Schindelin et al., 2012). For α measurements, two circles were fitted inside the chamber apex of atrium and ventricle, close to the AVC in a way that the diameter of each circle was defined by the chamber width. The connection between the two central points of these circles and the center of the inflow tract defined the looping angle, α (see scheme in Fig. 1G). For the index value (a/b), the ratio a/b was calculated, where a is the entire heart length and b is the distance between atrial and ventricular apex (see scheme in Fig. 1I). If not stated otherwise, looping angle and looping overlap were measured on confocal images of extracted hearts from fixed embryos (positioned in a plane). The looping overlap was also measured on confocal images of hearts from embedded embryos. For quantifying the relative dmKO2 fluorescent intensity in *Tg(BRE:dmKO2)^{mw40}* embryos, dissected hearts were mounted in SlowFade Gold (Invitrogen, S36936) and imaged on a LSM 510 META NLO confocal microscope (Zeiss) with a LD C-Apochromat 40×/1.1 W korr UV-VIS-IR M27 objective using the same setting for all samples. Frontal cross-section planes comprising superior and inferior AVC (marked by ALCAM-positive endocardial cells) were acquired using the oblique slicer tool in Imaris (Bitplane). Fluorescent dmKO2 intensity was measured within the cross-section area of around five myocardial cells positioned centrally in superior or inferior AVC using the free-hand selection tool in Fiji (Schindelin et al., 2012). Fluorescence intensity is shown as relative to the mean signal intensity within the superior AVC of control hearts, which is defined as 100%. A similar approach was used to measure relative P-Smad1/5/8 immunohistochemical staining intensities.

Quantifications of myocardial cell surface area and shape

To allow assessment of cell morphologies, myocardial cell borders were outlined with an antibody against the cell adhesion protein ALCAM (see Immunohistochemistry section) or measured from multicolor mosaic-labelled hearts. Fiji software (Schindelin et al., 2012) was used to quantify the morphological parameters. Cell surface area and shape were calculated as was described by Dietrich et al. (2014). Cell surface areas are shown relative to the RLV region at 32 hpf. Cell shape values are from 0.1 to 1, where a value of 0.1 characterizes an elongated cell and a value of 1.0 corresponds with a perfect circle.

Heart torsion calculations

We selected six cross-section planes of fluorescence projection images (Imaris software, Bitplane) perpendicular to the mid-sagittal plane of the mosaically labelled 48 hpf heart with an even distribution throughout ventricle and atrium. Uniquely identifiable cardiomyocytes within selected cross-section planes were then matched to cross-section planes of earlier and later stages (40 and 54 hpf). The matching rings were selected in a way that they were perpendicular to the centerline of the heart and contained the maximum number of tracked cells. Embryos were extracted from agarose after imaging each time point to ensure physiological heart development, which results in a change of heart orientation for the next round of imaging. In-order to keep the quantification consistent at all time-points, it is important to first orient the images acquired from the hearts before performing any analysis. A customized Matlab-based software was used for orienting the heart at different time points. Briefly, to normalize changes in orientation of the heart at different stages, we selected a reference cross-section plane of the 40 hpf atrium (section plane 2). For each stage, plane number 2 was rotated gradually and we calculated the Pearson correlation coefficient between the 40 hpf reference plane and the rotated reference plane at all other stages. The rotation angle, at which this correlation coefficient is maximum, was selected to adjust all stage-matched section planes.

In the oriented hearts, the angle (θ_{ipc}) of each cell (c_j) at the polar coordinate (with the reference point being the cross-section of the centerline of the heart tube with the plane and the reference direction being the right side) was calculated for all the cells contained in each of the section planes (p_i) at each time-point (t_k). A custom Matlab-based software was designed for this purpose.

The angular shift for each cell is defined as:

$$\rho_{kij} = \theta_{i_k p_i c_j} - \theta_{i_{k-1} p_i c_j},$$

where ρ is the angular shift, θ is the angle, c_j is the j^{th} cell, p_i is the i^{th} plane and t_k is the k^{th} time point. A value of $\rho_{kij} > 0$, indicates a counterclockwise (leftward) rotation of the plane, and $\rho_{kij} < 0$ means a clockwise (rightward) rotation of the j^{th} cell of the i^{th} plane at time t_k . If all of the cells of the i^{th} plane have a positive or negative angular shift, it means that the i^{th} ring is rotated.

We define torsion as:

$$\tau_{mn} = \frac{\sum_{i=1}^{I_m} \rho_{kim}}{I_m} - \frac{\sum_{i=1}^{I_n} \rho_{kin}}{I_n},$$

where τ_{mn} is the torsion between planes m and n , I_m is the number of cells in the m^{th} plane, and I_n is the number of cells in the n^{th} plane.

Statistical analysis

All experiments were performed in at least three independent biological replicates. All data are presented as mean ± standard deviation (s.d.). Statistical analysis was carried out using PRISM Graph Pad software. D'Agostino & Pearson omnibus normality test ($\alpha=0.05$) was used to check for parametric or non-parametric distribution. For parametric distribution, a one-way ANOVA Holm-Sidak test was used. For non-parametric distribution, Kruskal–Wallis or Dunn's test were used. Significance levels for multiple comparisons were assigned by PRISM based on mean rank differences or mean differences, respectively. ns, not significant; * $P \leq 0.05$, ** $P \leq 0.01$, *** $P \leq 0.001$ and **** $P \leq 0.0001$.

Acknowledgements

For critical reading of the manuscript we are indebted to R. Hodge and members of our team. We thank Nina Armbrecht and Anne Kühnel for support with fish husbandry, and Didier Stainier, Jeroen Bakkers, Brian Link and Matthias Hammerschmidt for sharing zebrafish or reagents. Part of this manuscript contains extracts from Melina Heise's PhD thesis (Hannover Medical School) entitled 'Morphogenetic control of zebrafish cardiac looping by Bmp signaling'.

Competing interests

The authors declare no competing or financial interests.

Author contributions

Conceptualization: V.A.L., M.H., J.M., S.A.-S.; Methodology: V.A.L., M.H., M.M., D.B., S.A.-S.; Software: V.A.L., M.H., M.M.; Validation: V.A.L., M.H., S.A.-S.; Formal analysis: V.A.L., M.H., M.M., D.B., J.M., S.A.-S.; Investigation: V.A.L., M.H., M.M., D.B., S.A.-S.; Resources: S.A.-S.; Data curation: V.A.L., M.H., M.M., J.M., S.A.-S.; Writing - original draft: V.A.L., M.H., J.M., S.A.-S.; Writing - review & editing: V.A.L., S.A.-S.; Visualization: V.A.L., M.H., M.M., J.M., S.A.-S.; Supervision: V.A.L., S.A.-S.; Project administration: V.A.L., S.A.-S.; Funding acquisition: S.A.-S.

Funding

V.A.L. acknowledges the Consejo Nacional de Investigaciones Científicas y Técnicas (CONICET) for support. M.H. was supported by a fellowship from the Excellence cluster REBIRTH and by a fellowship by the Joachim Herz Stiftung. S.A.-S. was supported by the Excellence cluster REBIRTH, by the Deutsche Zentrum für Herz-Kreislauf-Forschung (SFB958) and by Deutsche Forschungsgemeinschaft (SE2016/7-2 and SE2016/10-1).

Supplementary information

Supplementary information available online at <http://dev.biologists.org/lookup/doi/10.1242/dev.180091.supplemental>

References

- Abu-Daya, A., Sater, A. K., Wells, D. E., Mohun, T. J. and Zimmerman, L. B. (2009). Absence of heartbeat in the *Xenopus tropicalis* mutation muzak is caused by a nonsense mutation in cardiac myosin myh6. *Dev. Biol.* **336**, 20-29. doi:10.1016/j.ydbio.2009.09.019
- Auman, H. J., Coleman, H., Riley, H. E., Olale, F., Tsai, H.-J. and Yelon, D. (2007). Functional modulation of cardiac form through regionally confined cell shape changes. *PLoS Biol.* **5**, e53. doi:10.1371/journal.pbio.0050053
- Bacon, R. L. (1945). Self-differentiation and induction of the heart of *Amblystoma*. *J. Exp. Zool.* **98**, 87-125. doi:10.1002/jez.1400980202
- Bajolle, F., Zaffran, S., Kelly, R. G., Hadchouel, J., Bonnet, D., Brown, N. A. and Buckingham, M. E. (2006). Rotation of the myocardial wall of the outflow tract is implicated in the normal positioning of the great arteries. *Circ. Res.* **98**, 421-428. doi:10.1161/01.RES.0000202800.85341.6e
- Baker, K., Holtzman, N. G. and Burdine, R. D. (2008). Direct and indirect roles for Nodal signaling in two axis conversions during asymmetric morphogenesis of the zebrafish heart. *Proc. Natl. Acad. Sci. USA* **105**, 13924-13929. doi:10.1073/pnas.0802159105
- Bakkers, J. (2011). Zebrafish as a model to study cardiac development and human cardiac disease. *Cardiovasc. Res.* **91**, 279-288. doi:10.1093/cvr/cvr098
- Bayraktar, M. and Männer, J. (2014). Cardiac looping may be driven by compressive loads resulting from unequal growth of the heart and pericardial cavity. Observations on a physical simulation model. *Front. Physiol.* **5**, 112. doi:10.3389/fphys.2014.00112
- Breckenridge, R. A., Mohun, T. J. and Amaya, E. (2001). A role for BMP signalling in heart looping morphogenesis in *Xenopus*. *Dev. Biol.* **232**, 191-203. doi:10.1006/dbio.2001.0164
- Brennan, J., Norris, D. P. and Robertson, E. J. (2002). Nodal activity in the node governs left-right asymmetry. *Genes Dev.* **16**, 2339-2344. doi:10.1101/gad.1016202
- Burdine, R. D. and Schier, A. F. (2000). Conserved and divergent mechanisms in left-right axis formation. *Genes Dev.* **14**, 763-776.
- Butler, J. K. (1952). An experimental analysis of cardiac loop formation in the chick. *MA thesis*, University of Texas, Austin, TX.
- Chen, J. N., van Eeden, F. J., Warren, K. S., Chin, A., Nusslein-Volhard, C., Haffter, P. and Fishman, M. C. (1997). Left-right pattern of cardiac BMP4 may drive asymmetry of the heart in zebrafish. *Development* **124**, 4373-4382.
- Chen, C.-M., Norris, D. and Bhattacharya, S. (2010). Transcriptional control of left-right patterning in cardiac development. *Pediatr. Cardiol.* **31**, 371-377. doi:10.1007/s00246-009-9610-3
- Chi, N. C., Shaw, R. M., De Val, S., Kang, G., Jan, L. Y., Black, B. L. and Stainier, D. Y. R. (2008). Foxn4 directly regulates tbx2b expression and atrioventricular canal formation. *Genes Dev.* **22**, 734-739. doi:10.1101/gad.1629408
- Chocron, S., Verhoeven, M. C., Rentzsch, F., Hammerschmidt, M. and Bakkers, J. (2007). Zebrafish Bmp4 regulates left-right asymmetry at two distinct developmental time points. *Dev. Biol.* **305**, 577-588. doi:10.1016/j.ydbio.2007.03.001
- Christoffels, V. M., Habets, P. E. M. H., Franco, D., Campione, M., de Jong, F., Lamers, W. H., Bao, Z.-Z., Palmer, S., Biben, C., Harvey, R. P. et al. (2000). Chamber formation and morphogenesis in the developing mammalian heart. *Dev. Biol.* **223**, 266-278. doi:10.1006/dbio.2000.9753
- Collery, R. F. and Link, B. A. (2011). Dynamic smad-mediated BMP signaling revealed through transgenic zebrafish. *Dev. Dyn.* **240**, 712-722. doi:10.1002/dvdy.22567
- Cuny, G. D., Yu, P. B., Laha, J. K., Xing, X., Liu, J.-F., Lai, C. S., Deng, D. Y., Sachidanandan, C., Bloch, K. D. and Peterson, R. T. (2008). Structure-activity relationship study of bone morphogenetic protein (BMP) signaling inhibitors. *Bioorg. Med. Chem. Lett.* **18**, 4388-4392. doi:10.1016/j.bmcl.2008.06.052
- Deacon, D. C., Nevis, K. R., Cashman, T. J., Zhou, Y., Zhao, L., Washko, D., Guner-Ataman, B., Burns, C. G. and Burns, C. E. (2010). The miR-143-adducin3 pathway is essential for cardiac chamber morphogenesis. *Development* **137**, 1887-1896. doi:10.1242/dev.050526
- de Pater, E., Clijsters, L., Marques, S. R., Lin, Y. F., Garavito-Aguilar, Z. V., Yelon, D. and Bakkers, J. (2009). Distinct phases of cardiomyocyte differentiation regulate growth of the zebrafish heart. *Development* **136**, 1633-1641. doi:10.1242/dev.030924
- Dietrich, A.-C., Lombardo, V. A., Veerkamp, J., Priller, F. and Abdelilah-Seyfried, S. (2014). Blood flow and Bmp signaling control endocardial chamber morphogenesis. *Dev. Cell* **30**, 367-377. doi:10.1016/j.devcel.2014.06.020
- Ekman, G. (1925). Experimentelle Beiträge zur Herzentwicklung der Amphibien. *Wilhelm Roux Arch. Entwickl. Mech. Org.* **106**, 320-352. doi:10.1007/BF02079537
- Fransen, M. E. and Lemanski, L. F. (1988). Myocardial cell relationships during morphogenesis in normal and cardiac lethal mutant axolotls, *Ambystoma mexicanum*. *Am. J. Anat.* **183**, 245-257. doi:10.1002/aja.1001830307
- Galloway, J. L., Wingert, R. A., Thisse, C., Thisse, B. and Zon, L. I. (2005). Loss of *gata1* but not *gata2* converts erythropoiesis to myelopoiesis in zebrafish embryos. *Dev. Cell* **8**, 109-116. doi:10.1016/j.devcel.2004.12.001
- Grimes, D. T. and Burdine, R. D. (2017). Left-right patterning: breaking symmetry to asymmetric morphogenesis. *Trends Genet.* **33**, 616-628. doi:10.1016/j.tig.2017.06.004
- Hami, D., Grimes, A. C., Tsai, H.-J. and Kirby, M. L. (2011). Zebrafish cardiac development requires a conserved secondary heart field. *Development* **138**, 2389-2398. doi:10.1242/dev.061473
- Huang, C.-J., Tu, C.-T., Hsiao, C.-D., Hsieh, F.-J. and Tsai, H.-J. (2003). Germ-line transmission of a myocardium-specific GFP transgene reveals critical regulatory elements in the cardiac myosin light chain 2 promoter of zebrafish. *Dev. Dyn.* **228**, 30-40. doi:10.1002/dvdy.10356
- Huang, W., Zhang, R. and Xu, X. (2009). Myofibrillogenesis in the developing zebrafish heart: A functional study of *tnt2*. *Dev. Biol.* **331**, 237-249. doi:10.1016/j.ydbio.2009.04.039
- Jiao, K., Kullessa, H., Thompkins, K., Zhou, Y., Batts, L., Baldwin, H. S. and Hogan, B. L. M. (2003). An essential role of Bmp4 in the atrioventricular septation of the mouse heart. *Genes Dev.* **17**, 2362-2367. doi:10.1101/gad.1124803
- Jidigam, V. K., Srinivasan, R. C., Pattthy, C. and Gunhaga, L. (2015). Apical constriction and epithelial invagination are regulated by BMP activity. *Biol. Open* **4**, 1782-1791. doi:10.1242/bio.015263
- Jin, S.-W., Beis, D., Mitchell, T., Chen, J. N. and Stainier, D. Y. (2005). Cellular and molecular analyses of vascular tube and lumen formation in zebrafish. *Development* **132**, 5199-5209. doi:10.1242/dev.02087
- Kawakami, K. (2007). Tol2: a versatile gene transfer vector in vertebrates. *Genome Biol.* **8** Suppl. 1, S7. doi:10.1186/gb-2007-8-s1-s7
- Kelly, R. G., Buckingham, M. E. and Moorman, A. F. (2014). Heart fields and cardiac morphogenesis. *Cold Spring Harb. Perspect. Med.* **4**, a015750. doi:10.1101/cshperspect.a015750
- Kidokoro, H., Okabe, M. and Tamura, K. (2008). Time-lapse analysis reveals local asymmetrical changes in C-looping heart tube. *Dev. Dyn.* **237**, 3545-3556. doi:10.1002/dvdy.21662
- Latacha, K. S., Rémond, M. C., Ramasubramanian, A., Chen, A. Y., Elson, E. L. and Taber, L. A. (2005). Role of actin polymerization in bending of the early heart tube. *Dev. Dyn.* **233**, 1272-1286. doi:10.1002/dvdy.20488
- Le Garrec, J. F., Dominguez, J. N., Desgrange, A., Ivanovitch, K. D., Raphael, E., Bangham, J. A., Torres, M., Coen, E., Mohun, T. J. and Meilhac, S. M. (2017). A predictive model of asymmetric morphogenesis from 3D reconstructions of mouse heart looping dynamics. *Elife* **6**, e28951. doi:10.7554/eLife.28951
- Lenhart, K. F., Holtzman, N. G., Williams, J. R. and Burdine, R. D. (2013). Integration of nodal and BMP signals in the heart requires FoxH1 to create left-right differences in cell migration rates that direct cardiac asymmetry. *PLoS Genet.* **9**, e1003109. doi:10.1371/journal.pgen.1003109
- Long, S., Ahmad, N. and Rebagliati, M. (2003). The zebrafish nodal-related gene southpaw is required for visceral and diencephalic left-right asymmetry. *Development* **130**, 2303-2316. doi:10.1242/dev.00436
- Lyons, S. E., Lawson, N. D., Lei, L., Bennett, P. E., Weinstein, B. M. and Liu, P. P. (2002). A nonsense mutation in zebrafish *gata1* causes the bloodless phenotype in vlad tepes. *Proc. Natl. Acad. Sci. USA* **99**, 5454-5459. doi:10.1073/pnas.082695299
- Ma, L., Lu, M. F., Schwartz, R. J. and Martin, J. F. (2005). Bmp2 is essential for cardiac cushion epithelial-mesenchymal transition and myocardial patterning. *Development* **132**, 5601-5611. doi:10.1242/dev.02156

- Manasek, F. J. and Monroe, R. G.** (1972). Early cardiac morphogenesis is independent of function. *Dev. Biol.* **27**, 584-588. doi:10.1016/0012-1606(72)90196-0
- Manasek, F. J., Burnside, M. B. and Waterman, R. E.** (1972). Myocardial cell shape change as a mechanism of embryonic heart looping. *Dev. Biol.* **29**, 349-371. doi:10.1016/0012-1606(72)90077-2
- Männer, J.** (2000). Cardiac looping in the chick embryo: a morphological review with special reference to terminological and biomechanical aspects of the looping process. *Anat. Rec.* **259**, 248-262. doi:10.1002/1097-0185(20000701)259:3<248::AID-AR30>3.0.CO;2-K
- Männer, J.** (2004). On rotation, torsion, lateralization, and handedness of the embryonic heart loop: new insights from a simulation model for the heart loop of chick embryos. *Anat. Rec. A Discov. Mol. Cell Evol. Biol.* **278**, 481-492. doi:10.1002/ar.a.20036
- Männer, J.** (2009). The anatomy of cardiac looping: a step towards the understanding of the morphogenesis of several forms of congenital cardiac malformations. *Clin. Anat.* **22**, 21-35. doi:10.1002/ca.20652
- Manning, A. and McLachlan, J. C.** (1990). Looping of chick embryo hearts in vitro. *J. Anat.* **168**, 257-263.
- Meilhac, S. M., Esner, M., Kerszberg, M., Moss, J. E. and Buckingham, M. E.** (2004). Oriented clonal cell growth in the developing mouse myocardium underlies cardiac morphogenesis. *J. Cell Biol.* **164**, 97-109. doi:10.1083/jcb.200309160
- Merks, A. M., Swinarski, M., Meyer, A. M., Müller, N. V., Özcan, I., Donat, S., Burger, A., Gilbert, S., Mosimann, C., Abdellilah-Seyfried, S. et al.** (2018). Planar cell polarity signalling coordinates heart tube remodelling through tissue-scale polarisation of actomyosin activity. *Nat. Commun.* **9**, 2161. doi:10.1038/s41467-018-04566-1
- Nasevicius, A. and Ekker, S. C.** (2000). Effective targeted gene 'knockdown' in zebrafish. *Nat. Genet.* **26**, 216-220. doi:10.1038/79951
- Nerurkar, N. L., Mahadevan, L. and Tabin, C. J.** (2017). BMP signaling controls buckling forces to modulate looping morphogenesis of the gut. *Proc. Natl. Acad. Sci. USA* **114**, 2277-2282. doi:10.1073/pnas.1700307114
- Noël, E. S., Verhoeven, M., Legendijk, A. K., Tessadori, F., Smith, K., Choorapoikayil, S., den Hertog, J. and Bakkers, J.** (2013). A Nodal-independent and tissue-intrinsic mechanism controls heart-looping chirality. *Nat. Commun.* **4**, 2754. doi:10.1038/ncomms3754
- Nusse, R.** (2005). Wnt signaling in disease and in development. *Cell Res.* **15**, 28-32. doi:10.1038/sj.cr.7290260
- Ocaña, O. H., Coskun, H., Minguilón, C., Murawala, P., Tanaka, E. M., Galcerán, J., Muñoz-Chápuli, R. and Nieto, M. A.** (2017). A right-handed signalling pathway drives heart looping in vertebrates. *Nature* **549**, 86-90. doi:10.1038/nature23454
- Paolini, A. and Abdellilah-Seyfried, S.** (2018). The mechanobiology of zebrafish cardiac valve leaflet formation. *Curr. Opin. Cell Biol.* **55**, 52-58. doi:10.1016/j.cob.2018.05.007
- Patten, B. M.** (1922). The formation of the cardiac loop in the chick. *Am. J. Anat.* **30**, 373-397. doi:10.1002/aja.1000300304
- Rajagopal, R., Huang, J., Dattilo, L. K., Kaartinen, V., Mishina, Y., Deng, C.-X., Umans, L., Zwijsen, A., Roberts, A. B. and Beebe, D. C.** (2009). The type I BMP receptors, *Bmpr1a* and *Acvr1*, activate multiple signaling pathways to regulate lens formation. *Dev. Biol.* **335**, 305-316. doi:10.1016/j.ydbio.2009.08.027
- Ramsdell, A. F.** (2005). Left-right asymmetry and congenital cardiac defects: getting to the heart of the matter in vertebrate left-right axis determination. *Dev. Biol.* **288**, 1-20. doi:10.1016/j.ydbio.2005.07.038
- Rebagliati, M. R., Toyama, R., Fricke, C., Haffter, P. and Dawid, I. B.** (1998). Zebrafish nodal-related genes are implicated in axial patterning and establishing left-right asymmetry. *Dev. Biol.* **199**, 261-272. doi:10.1006/dbio.1998.8935
- Risebro, C. A., Smart, N., Dupays, L., Breckenridge, R., Mohun, T. J. and Riley, P. R.** (2006). Hand1 regulates cardiomyocyte proliferation versus differentiation in the developing heart. *Development* **133**, 4595-4606. doi:10.1242/dev.02625
- Sanvitale, C. E., Kerr, G., Chaikwad, A., Ramel, M.-C., Mohedas, A. H., Reichert, S., Wang, Y., Triffitt, J. T., Cuny, G. D., Yu, P. B. et al.** (2013). A new class of small molecule inhibitor of BMP signaling. *PLoS ONE* **8**, e62721. doi:10.1371/journal.pone.0062721
- Schindelin, J., Arganda-Carreras, I., Frise, E., Kaynig, V., Longair, M., Pietzsch, T., Preibisch, S., Rueden, C., Saalfeld, S., Schmid, B. et al.** (2012). Fiji: an open-source platform for biological-image analysis. *Nat. Methods* **9**, 676-682. doi:10.1038/nmeth.2019
- Schindler, Y. L., Garske, K. M., Wang, J., Firulli, B. A., Firulli, A. B., Poss, K. D. and Yelon, D.** (2014). Hand2 elevates cardiomyocyte production during zebrafish heart development and regeneration. *Development* **141**, 3112-3122. doi:10.1242/dev.106336
- Sehnert, A. J., Huq, A., Weinstein, B. M., Walker, C., Fishman, M. and Stainier, D. Y. R.** (2002). Cardiac tropinin T is essential in sarcomere assembly and cardiac contractility. *Nat. Genet.* **31**, 106-110. doi:10.1038/ng875
- Shi, Y., Yao, J., Xu, G. and Taber, L. A.** (2014a). Bending of the looping heart: differential growth revisited. *J. Biomech. Eng.* **136**, 081002. doi:10.1115/1.4026645
- Shi, Y., Yao, J., Young, J. M., Fee, J. A., Perucchio, R. and Taber, L. A.** (2014b). Bending and twisting the embryonic heart: a computational model for c-looping based on realistic geometry. *Front. Physiol.* **5**, 297. doi:10.3389/fphys.2014.00297
- Singleman, C. and Holtzman, N. G.** (2012). Analysis of postembryonic heart development and maturation in the zebrafish, *Danio rerio*. *Dev. Dyn.* **241**, 1993-2004. doi:10.1002/dvdy.23882
- Smith, K. A., Chocron, S., von der Hardt, S., de Pater, E., Soufan, A., Bussmann, J., Schulte-Merker, S., Hammerschmidt, M. and Bakkers, J.** (2008). Rotation and asymmetric development of the zebrafish heart requires directed migration of cardiac progenitor cells. *Dev. Cell* **14**, 287-297. doi:10.1016/j.devcel.2007.11.015
- Smith, K. A., Noël, E., Thurlings, I., Rehmann, H., Chocron, S. and Bakkers, J.** (2011). Bmp and nodal independently regulate *lefty1* expression to maintain unilateral nodal activity during left-right axis specification in zebrafish. *PLoS Genet.* **7**, e1002289. doi:10.1371/journal.pgen.1002289
- Somi, S., Buffing, A. A. M., Moorman, A. F. M. and Van Den Hoff, M. J. B.** (2004). Dynamic patterns of expression of BMP isoforms 2, 4, 5, 6, and 7 during chicken heart development. *Anat. Rec. A Discov. Mol. Cell Evol. Biol.* **279**, 636-651. doi:10.1002/ar.a.20031
- Soufan, A. T., van den Berg, G., Ruijter, J. M., de Boer, P. A. J., van den Hoff, M. J. B. and Moorman, A. F. M.** (2006). Regionalized sequence of myocardial cell growth and proliferation characterizes early chamber formation. *Circ. Res.* **99**, 545-552. doi:10.1161/01.RES.0000239407.45137.97
- Srivastava, D., Thomas, T., Lin, Q., Kirby, M. L., Brown, D. and Olson, E. N.** (1997). Regulation of cardiac mesodermal and neural crest development by the bHLH transcription factor, dHAND. *Nat. Genet.* **16**, 154-160. doi:10.1038/ng0697-154
- Staudt, D. W., Liu, J., Thorn, K. S., Stuurman, N., Liebling, M. and Stainier, D. Y. R.** (2014). High-resolution imaging of cardiomyocyte behavior reveals two distinct steps in ventricular trabeculation. *Development* **141**, 585-593. doi:10.1242/dev.098632
- Taber, L. A.** (2006). Biophysical mechanisms of cardiac looping. *Int. J. Dev. Biol.* **50**, 323-332. doi:10.1387/ijdb.052045lt
- Taber, L. A., Voronov, D. A. and Ramasubramanian, A.** (2010). The role of mechanical forces in the torsional component of cardiac looping. *Ann. N. Y. Acad. Sci.* **1188**, 103-110. doi:10.1111/j.1749-6632.2009.05089.x
- Thompson, R. P., Abercrombie, V. and Wong, M.** (1987). Morphogenesis of the truncus arteriosus of the chick embryo heart: movements of autoradiographic tattoos during septation. *Anat. Rec.* **218**, 434-440, 394-395. doi:10.1002/ar.1092180411
- Tsai, F.-Y. and Orkin, S. H.** (1997). Transcription factor GATA-2 is required for proliferation/survival of early hematopoietic cells and mast cell formation, but not for erythroid and myeloid terminal differentiation. *Blood* **89**, 3636-3643. doi:10.1182/blood.V89.10.3636
- Veerkamp, J., Rudolph, F., Cseresnyes, Z., Priller, F., Otten, C., Renz, M., Schaefer, L. and Abdellilah-Seyfried, S.** (2013). Unilateral dampening of Bmp activity by nodal generates cardiac left-right asymmetry. *Dev. Cell* **24**, 660-667. doi:10.1016/j.devcel.2013.01.026
- Vermot, J., Forouhar, A. S., Liebling, M., Wu, D., Plummer, D., Gharib, M. and Fraser, S. E.** (2009). Reversing blood flows act through *kif2a* to ensure normal valvulogenesis in the developing heart. *PLoS Biol.* **7**, e1000246. doi:10.1371/journal.pbio.1000246
- Vincent, S. D., Norris, D. P., Le Good, J. A., Constam, D. B. and Robertson, E. J.** (2004). Asymmetric Nodal expression in the mouse is governed by the combinatorial activities of two distinct regulatory elements. *Mech. Dev.* **121**, 1403-1415. doi:10.1016/j.mod.2004.06.002
- Voronov, D. A., Alford, P. W., Xu, G. and Taber, L. A.** (2004). The role of mechanical forces in dextral rotation during cardiac looping in the chick embryo. *Dev. Biol.* **272**, 339-350. doi:10.1016/j.ydbio.2004.04.033
- Walsh, E. C. and Stainier, D. Y.** (2001). UDP-glucose dehydrogenase required for cardiac valve formation in zebrafish. *Science* **293**, 1670-1673. doi:10.1126/science.293.5535.1670
- Weber, M., Scherf, N., Meyer, A. M., Panakova, D., Kohl, P. and Huisken, J.** (2017). Cell-accurate optical mapping across the entire developing heart. *Elife* **6**, e28307. doi:10.7554/eLife.28307
- Westerfield, M.** (2007). *The Zebrafish Book. A Guide for the Laboratory Use of Zebrafish (Danio rerio)*, 5th edn. Eugene, OR: University of Oregon Press.
- Widmann, T. J. and Dahmann, C.** (2009). Dpp signaling promotes the cuboidal-to-columnar shape transition of *Drosophila* wing disc epithelia by regulating Rho1. *J. Cell Sci.* **122**, 1362-1373. doi:10.1242/jcs.044271
- Yamada, M., Revelli, J.-P., Eichele, G., Barron, M. and Schwartz, R. J.** (2000). Expression of chick *Tbx-2*, *Tbx-3*, and *Tbx-5* genes during early heart development: evidence for BMP2 induction of *Tbx-2*. *Dev. Biol.* **228**, 95-105. doi:10.1006/dbio.2000.9927
- Yamaguchi, T. P.** (2001). Heads or tails: Wnts and anterior-posterior patterning. *Curr. Biol.* **11**, R713-R724. doi:10.1016/S0960-9822(01)00417-1
- Zhang, H. and Bradley, A.** (1996). Mice deficient for BMP2 are nonviable and have defects in amnion/chorion and cardiac development. *Development* **122**, 2977-2986.
- Zhou, Y., Cashman, T. J., Nevis, K. R., Obregon, P., Carney, S. A., Liu, Y., Gu, A., Mosimann, C., Sondalle, S., Peterson, R. E. et al.** (2011). Latent TGF-beta binding protein 3 identifies a second heart field in zebrafish. *Nature* **474**, 645-648. doi:10.1038/nature10094

SUPPLEMENTARY INFORMATION

Table S1. S-looping parameter measurements of 54 hpf zebrafish hearts.

S-looped parameters	Mean \pm s.d.	N (hearts)	Statistical analysis		Sub-figure
			p-value [†]	p-value [‡]	
Looping angle (α) (°)					
(1) Wilde type	85 \pm 4	10			1H
(2) DMSO (0.2 %v/v)	77 \pm 12	24			3K
(3) LDN193189 (20 μ M)	105 \pm 20	18	<0.001 (3 vs 2)	0.154 (3 vs 4)	3K
(4) K02288 (20 μ M)	98 \pm 16	27	<0.001 (4 vs 2)		3K
(5) Control	73 \pm 10	11			3S
(6) Mosaic Noggin3 clones	149 \pm 8	19	<0.001 (6 vs 5)	<0.001 (6 vs 8)	3S
(7) Hs:Noggin3	137 \pm 4	3	<0.001 (7 vs 5)	0.025 (6 vs 7)	3S
(8) Hs:Bmpb2	130 \pm 4	4	<0.001 (8 vs 5)	0.273 (7 vs 8)	3S
(9) DMSO (0.1 %v/v)	84 \pm 20	19			4J
(10) IWR-1 (20 μ M)	83 \pm 19	15	0.883 (10 vs 9)		4J
(11) control MO	82 \pm 5	5			5G
(12) MO <i>Gata1</i>	95 \pm 10	4	0.172 (12 vs 11)	0.071 (12 vs 14)	5G
(13) MO <i>Gata2</i>	103 \pm 13	3	0.051 (13 vs 11)	0.361 (13 vs 14)	5G
(14) MO <i>Gata1/gata2</i>	112 \pm 19	6	0.002 (14 vs 11)	0.450 (12 vs 13)	5G
(15) MO <i>tnnt2a</i>	135 \pm 24	14	<0.001 (15 vs 11)		5G
(16) control	93 \pm 8	6			S6D
(17) <i>tnnt2a</i> ^{b109/b109}	125 \pm 15	8	<0.001 (17 vs 16)		S6D
Looping overlap (Index a/b)					
(1) Wilde type	2.2 \pm 0.2	7			1J
(2) DMSO (0.2 %v/v)	2.2 \pm 0.7	24			3L
(3) LDN193189 (20 μ M)	4.3 \pm 2.6	18	<0.001 (3 vs 2)	0.064 (3 vs 4)	3L
(4) K02288 (20 μ M)	3.3 \pm 1.7	27	0.028 (4 vs 2)		3L
(5) control	1.9 \pm 0.4	6			3T
(6) Mosaic Noggin3 clones	14 \pm 8	12	<0.001 (6 vs 5)	0.066 (6 vs 8)	3T
(7) Hs:Noggin3	9 \pm 8	3	0.136 (7 vs 5)	0.244 (6 vs 7)	3T
(8) Hs:Bmpb2	5.9 \pm 0.8	3	0.391 (8 vs 5)	0.563 (7 vs 8)	3T
(9) D-loop <i>spaw</i> MO	2.3 \pm 0.4	3	0.656 (9 vs 1)	<0.001 (9 vs 11)	4G
(10) L-loop <i>spaw</i> MO	2.4 \pm 0.4	5	0.465 (10 vs 1)	<0.001 (10 vs 11)	4G
(11) V-loop <i>spaw</i> MO	5.4 \pm 0.7	5	<0.001 (11 vs 1)	0.866 (9 vs 10)	4G
(12) DMSO (0.1 %v/v)	2.9 \pm 1.0	19			4K
(13) IWR-1 (20 μ M)	2.8 \pm 1.4	15	0.81 (13 vs 12)		4K
(14) Control	2.1 \pm 0.2	5			5H
(15) <i>Gata1</i> MO	3.1 \pm 0.3	4	0.150 (15 vs 14)	0.027 (15 vs 17)	5H
(16) <i>Gata2</i> MO	3.4 \pm 0.7	3	0.096 (16 vs 14)	0.084 (16 vs 17)	5H
(17) <i>Gata1/gata2</i> MO	4.6 \pm 1.6	6	<0.001 (17 vs 14)	0.718 (15 vs 16)	5H
(18) MO <i>tnnt2a</i>	8.0 \pm 4.2	14	<0.001 (18 vs 14)		5H
(19) control	2.1 \pm 0.3	6			S6E
(20) <i>tnnt2a</i> ^{b109/b109}	9.6 \pm 3.5	7	<0.001 (20 vs 19)		S6E

[†] comparison between samples and control; [‡] comparison between samples. One Way ANOVA - Holm-Sidak method was used for all statistical analysis. Different experiments are separated by a line.

Table S2. Torsional winding analysis.(A) Angular shifts of selected planes along the heart tube during S-looping morphogenesis. (B) Statistical analysis of angular shift differences between planes. Related to Fig. 1M,N,O.

A

Angular shifts (°)	Plane 1		Plane 2		Plane 3		Plane 4		Plane 5		Plane 6	
	mean ± s.d. (°)	n	mean ± s.d. (°)	n	mean ± s.d. (°)	n	mean ± s.d. (°)	n	mean ± s.d. (°)	n	mean ± s.d. (°)	n
40-48 hpf	7.8 ± 13.7	20	3.2 ± 13.1	18	2.4 ± 20.5	22	-7.7 ± 12.7	15	-2.4 ± 11.9	9	8.4 ± 17.9	8
48-54 hpf	3.5 ± 17.0	20	8.8 ± 19.0	18	-4.6 ± 10.5	23	-1.5 ± 23.3	15	-34.7 ± 25.2	9	-51.0 ± 41.2	8
40-54 hpf	11.3 ± 28.6	20	12.0 ± 26.6	18	-2.3 ± 24.1	23	-9.1 ± 28.2	15	-37.1 ± 30.6	9	-42.6 ± 35.7	8

n, number of myocardial cell analyzed for 3 hearts.

B

Statistical analysis†	40-48 hpf		48-54 hpf		40-54 hpf	
	mean rank. diff. ‡	p-value	mean rank. diff. ‡	p-value	mean rank. diff. ‡	p-value
Plane 1 vs Plane 2	8.87	ns	-2.76	ns	2.56	ns
Plane 1 vs Plane 3	8.92	ns	13.76	ns	11.12	ns
Plane 1 vs Plane 4	26.55	ns	4.98	ns	19.55	ns
Plane 1 vs Plane 5	16.48	ns	37.29	< 0.01	39.17	< 0.01
Plane 1 vs Plane 6	-1.85	ns	41.48	< 0.01	43.7	< 0.01
Plane 2 vs Plane 3	0.05	ns	16.52	ns	8.56	ns
Plane 2 vs Plane 4	17.68	ns	7.74	ns	16.99	ns
Plane 2 vs Plane 5	7.61	ns	40.06	< 0.01	36.61	< 0.05
Plane 2 vs Plane 6	-10.72	ns	44.24	< 0.01	41.14	< 0.01
Plane 3 vs Plane 4	17.63	ns	-8.78	ns	8.43	ns
Plane 3 vs Plane 5	7.56	ns	23.53	ns	28.05	ns
Plane 3 vs Plane 6	-10.77	ns	27.71	ns	32.58	< 0.05
Plane 4 vs Plane 5	-10.07	ns	32.31	ns	19.62	ns
Plane 4 vs Plane 6	-28.40	ns	36.49	< 0.05	24.15	ns
Plane 5 vs Plane 6	-18.33	ns	4.18	ns	4.53	ns

†Kruskal-Wallis test, ‡mean ranking difference.

Table S3. Regional myocardial cell surface areas - Statistical analysis

Myocardial cell surface areas - heart chamber regions	32 hpf		40 hpf		48 hpf		54 hpf	
	Mean rank. diff.	Sign.	Mean rank. diff.	Sign.	Mean rank. diff.	Sign.	Mean rank. diff.	Sign.
RUV vs LUV	-	-	-	-	-10.69	ns	36.96	ns
RUV vs RLV	-	-	-	-	30.38	ns	31.81	ns
RUV vs LLV	-	-	-	-	81.75	P<0.05	59.07	ns
RUV vs AVC	-	-	-	-	-74.72	P<0.05	-45.13	ns
RUV vs RUA	-	-	-	-	29.80	ns	42.68	ns
RUV vs LUA	-	-	-	-	-61.11	ns	-60.16	ns
RUV vs RLA	-	-	-	-	-16.58	ns	4.84	ns
RUV vs LLA	-	-	-	-	-50.04	ns	-35.44	ns
LUV vs RLV	-	-	-	-	-41.06	ns	5.15	ns
LUV vs LLV	-	-	-	-	92.43	ns	22.11	ns
LUV vs AVC	-	-	-	-	-85.41	ns	-8.17	ns
LUV vs RUA	-	-	-	-	19.11	ns	79.63	ns
LUV vs LUA	-	-	-	-	50.42	ns	97.12	P<0.05
LUV vs RLA	-	-	-	-	-27.27	ns	41.80	ns
LUV vs LLA	-	-	-	-	39.36	ns	72.40	ns
RLV vs LLV	-	-	50.67	ns	51.37	ns	27.26	ns
RLV vs AVC	-	-	-28.56	ns	-44.34	ns	-13.32	ns
RLV vs RUA	-	-	49.82	ns	60.18	ns	74.48	P<0.001
RLV vs LUA	-	-	-26.17	ns	-91.49	P<0.0001	-91.97	P<0.0001
RLV vs RLA	-	-	30.73	ns	13.80	ns	36.65	ns
RLV vs LLA	-	-	-39.38	ns	-80.42	P<0.001	-67.25	P<0.001
LLV vs AVC	-	-	22.11	ns	7.03	ns	13.94	ns
LLV vs RUA	-	-	100.50	ns	111.50	P<0.001	101.70	P<0.0001
LLV vs LUA	-	-	76.84	ns	142.90	P<0.0001	119.20	P<0.0001
LLV vs RLA	-	-	81.40	ns	65.17	ns	63.91	P<0.05
LLV vs LLA	-	-	90.05	ns	131.80	P<0.0001	94.51	P<0.0001
AVC vs RUA	-39.40	P<0.05	-78.38	P<0.0001	-104.50	P<0.0001	-87.80	P<0.001
AVC vs LUA	-35.70	P<0.05	-54.74	P<0.001	-135.80	P<0.0001	-105.30	P<0.0001
AVC vs RLA	-29.53	ns	-59.29	P<0.01	-58.14	ns	-49.96	ns
AVC vs LLA	-32.16	ns	-67.94	P<0.001	-124.80	P<0.0001	-80.57	P<0.001
RUA vs LUA	3.70	ns	23.65	ns	-31.31	ns	-17.49	ns
RUA vs RLA	9.87	ns	19.09	ns	46.38	ns	37.84	ns
RUA vs LLA	7.24	ns	10.44	ns	-20.25	ns	7.23	ns
LUA vs RLA	-6.17	ns	4.55	ns	-77.69	P<0.001	-55.33	P<0.01
LUA vs LLA	3.54	ns	-13.21	ns	11.07	ns	24.72	ns
RLA vs LLA	-2.63	ns	-8.66	ns	-66.62	P<0.05	-30.60	ns

Three hearts were analyzed during cardiac looping morphogenesis at 32, 40, 48, and 54 hpf. Kruskal-Wallis test was used for multiple comparisons of myocardial cell surface areas within different heart chamber regions. Mean rank. diff. mean ranking difference; Sign. significance, undetermined; ns, not significant. Related to Fig. 2M.

Table S4. Regional myocardial cell circularities - Statistical analysis

Myocardial cell circularity - heart chamber regions	32 hpf		40 hpf		48 hpf		54 hpf	
	Mean rank. diff.	Sign.	Mean rank. diff.	Sign.	Mean rank. diff.	Sign.	Mean rank. diff.	Sign.
RUV vs LUV	-	-	-	-	-13.53	ns	-23.21	ns
RUV vs RLV	-	-	-	-	16.98	ns	-7.32	ns
RUV vs LLV	-	-	-	-	34.63	ns	-14.82	ns
RUV vs AVC	-	-	-	-	-106.20	P<0.0001	-56.55	ns
RUV vs RUA	-	-	-	-	-95.28	P<0.01	-40.85	ns
RUV vs LUA	-	-	-	-	35.68	ns	5.63	ns
RUV vs RLA	-	-	-	-	-120.00	P<0.0001	-83.88	P<0.05
RUV vs LLA	-	-	-	-	97.12	P<0.01	49.36	ns
LUV vs RLV	-	-	-	-	-30.51	ns	-15.89	ns
LUV vs LLV	-	-	-	-	48.16	ns	8.39	ns
LUV vs AVC	-	-	-	-	-119.80	P<0.001	-79.76	ns
LUV vs RUA	-	-	-	-	-108.80	P<0.05	-64.06	ns
LUV vs LUA	-	-	-	-	-49.21	ns	-28.84	ns
LUV vs RLA	-	-	-	-	-133.50	P<0.001	-107.10	P<0.01
LUV vs LLA	-	-	-	-	-110.60	P<0.01	-72.57	ns
RLV vs LLV	-	-	57.22	ns	17.65	ns	-7.50	ns
RLV vs AVC	-	-	-39.94	ns	-89.26	P<0.0001	-63.87	P<0.01
RLV vs RUA	-	-	-43.96	ns	-78.30	P<0.01	-48.17	ns
RLV vs LUA	-	-	5.35	ns	18.70	ns	12.95	ns
RLV vs RLA	-	-	-83.56	P<0.0001	-103.00	P<0.0001	-91.20	P<0.0001
RLV vs LLA	-	-	66.84	P<0.01	80.13	P<0.001	56.68	P<0.01
LLV vs AVC	-	-	17.28	ns	-71.61	P<0.05	-71.37	P<0.05
LLV vs RUA	-	-	13.26	ns	-60.65	ns	-55.67	ns
LLV vs LUA	-	-	51.87	ns	-1.05	ns	-20.45	ns
LLV vs RLA	-	-	-26.34	ns	-85.38	P<0.01	-98.69	P<0.0001
LLV vs LLA	-	-	-9.62	ns	-62.49	ns	-64.18	P<0.05
AVC vs RUA	39.52	P<0.05	4.02	ns	-10.96	ns	-15.70	ns
AVC vs LUA	14.70	ns	-34.59	ns	-70.56	P<0.001	-50.92	ns
AVC vs RLA	59.40	P<0.0001	43.62	ns	13.77	ns	27.33	ns
AVC vs LLA	35.20	ns	26.90	ns	-9.13	ns	-7.19	ns
RUA vs LUA	-24.81	ns	-38.61	ns	-59.60	ns	-35.22	ns
RUA vs RLA	19.89	ns	39.60	ns	24.73	ns	43.03	ns
RUA vs LLA	-4.32	ns	22.88	ns	1.84	ns	8.51	ns
LUA vs RLA	-44.70	P<0.001	-78.21	P<0.0001	-84.33	P<0.0001	-78.24	P<0.0001
LUA vs LLA	20.50	ns	61.49	P<0.001	61.43	P<0.05	43.73	ns
RLA vs LLA	-24.20	ns	-16.72	ns	-22.90	ns	-34.52	ns

Three hearts were analyzed during cardiac looping morphogenesis at 32, 40, 48, and 54 hpf. Kruskal-Wallis test was used for multiple comparisons of myocardial cell circularities within different heart chamber regions. Mean rank. diff. mean ranking difference; Sign. significance, undetermined; sn, not significant. Related to Fig. 2N.

Table S5. Relative dmKO2 fluorescence levels within myocardial AVC regions at 54 hpf.

Relative dmKO2 intensity	Mean \pm s.d. (%)	N (hearts)	Statistical analysis [†]		Sub-figure
			Diff of Ranks	significance	
Superior AVC					
(1) DMSO (0.2 %v/v)	100 \pm 32	12			3J
(2) LDN193189 (20 μ M)	71 \pm 25	7	28.49 (2 vs 1)	<0.05	3J
(3) K02288 (20 μ M)	57 \pm 28	12	43.42 (3 vs 1)	<0.001	3J
(4) Control	100 \pm 34	6			3R
(5) Mosaic Noggin3 clones	10 \pm 9	8	15.42 (5 vs 4)	<0.01	3R
(6) DMSO (0.1 %v/v)	100 \pm 30	17			4L
(7) IWR-1 (20 μ M)	72 \pm 27	14	13.63 (7 vs 6)	ns	4L
(8) Control MO	100 \pm 30	3			5F
(9) MO <i>Gata1</i>	59 \pm 27	4	9.17 (9 vs 8)	ns	5F
(10) MO <i>Gata2</i>	79 \pm 21	4	3.90 (10 vs 8)	ns	5F
(11) MO <i>Gata1/gata2</i>	60 \pm 7	3	8.33 (11 vs 8)	ns	5F
(12) MO <i>tnnt2a</i>	47 \pm 12	11	17.43 (12 vs 8)	<0.05	5F
Inferior AVC					
(1) DMSO (0.2 %v/v)	74 \pm 32	12			3J
(2) LDN193189 (20 μ M)	45 \pm 11	7	28.38 (2 vs 1)	<0.05	3J
(3) K02288 (20 μ M)	42 \pm 15	12	31.85 (3 vs 1)	<0.01	3J
(4) Control	66 \pm 32	6			3R
(5) Mosaic Noggin3 clones	10 \pm 8	8	12.58 (5 vs 4)	<0.01	3R
(6) DMSO (0.1 %v/v)	68 \pm 23	17			4L
(7) IWR-1 (20 μ M)	41 \pm 22	14	16.39 (7 vs 6)	<0.05	4L
(8) Control	56 \pm 4	3			5F
(9) MO <i>Gata1</i>	31 \pm 13	4	9.75 (9 vs 8)	ns	5F
(10) MO <i>Gata2</i>	39 \pm 11	4	6.00 (10 vs 8)	ns	5F
(11) MO <i>Gata1/gata2</i>	34 \pm 7	3	7.67 (11 vs 8)	ns	5F
(12) MO <i>tnnt2a</i>	42 \pm 14	11	9.95 (12 vs 8)	ns	5F

[†] comparison between samples and control. Kruskal-Wallis One Way Analysis of Variance on Ranks. All Pairwise Multiple Comparison Procedure (Dunn's Method) was used for statistical analysis. Different experiments are separated by a line.

Table S6. Relative P-Smad1/5/8 immunostaining levels within myocardial AVC region at 54 hpf.

	Mean \pm s.d.	N	Statistical analysis	
			p-value [†]	p-value [‡]
Superior AVC				
(1) Control	100 \pm 32	41		<0.001 (1 vs 3)
(2) <i>tnnt2a</i> ^{b109/b109}	47 \pm 19	18	<0.001 (1 vs 2)	<0.001 (1 vs 4)
Inferior AVC				
(3) Control	60 \pm 25	13		0.210 (3 vs 2)
(4) <i>tnnt2a</i> ^{b109/b109}	37 \pm 29	11	0.05 (3 vs 4)	0.358 (4 vs 2)

N, number of myocardial cells analyzed in four WT and three *tnnt2a*^{b109/b109} hearts. [†] comparison between mutant and control. [‡] comparison between samples. One Way ANOVA statistical analysis (Holm-Sidak method) was used. Related to Fig. S6C.

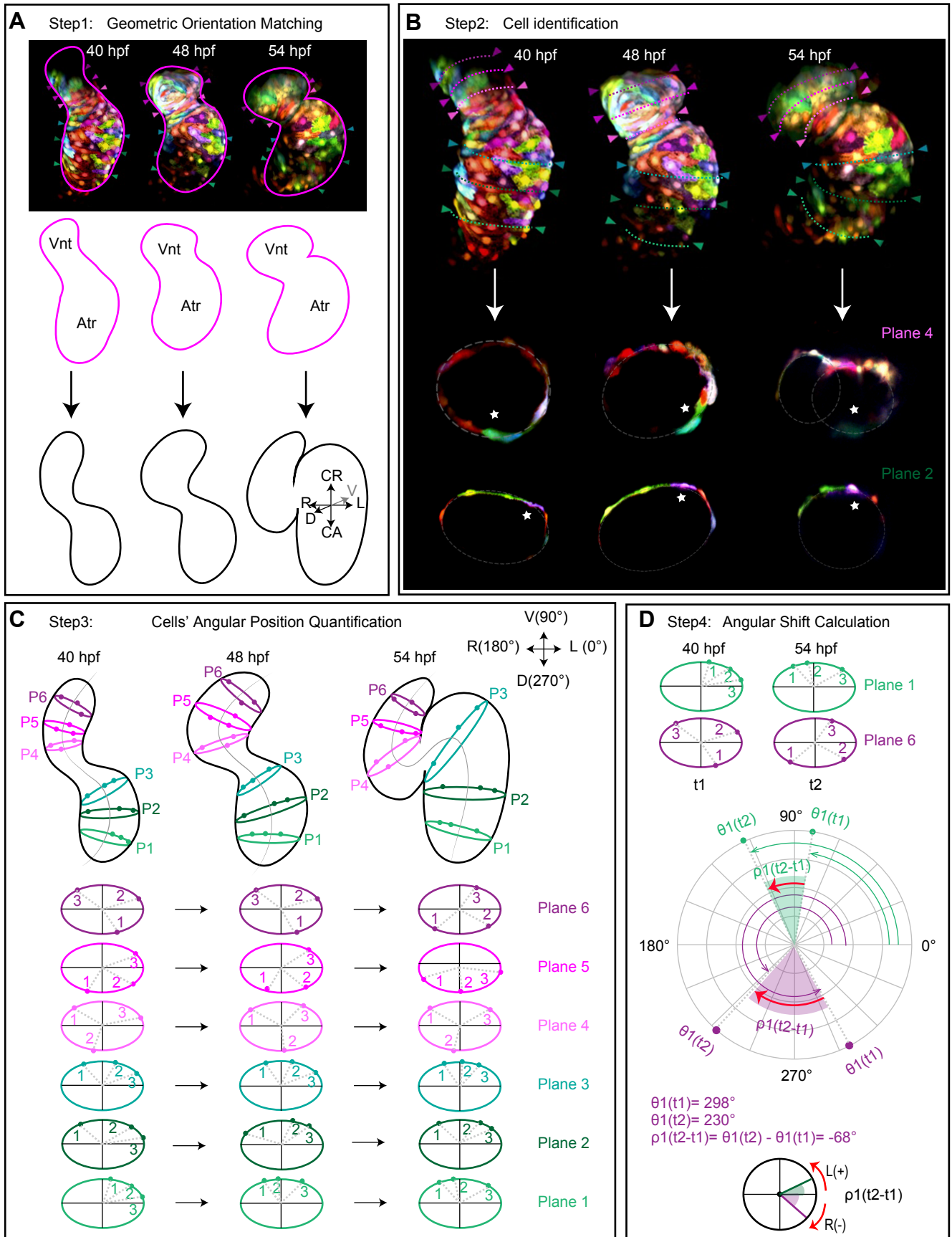


Fig. S1. Analysis of torsional deformation in a representative heart. (A) Step1: Normalization of the 3D images of the heart tube according to their respective geometric orientation at 48hpf. **(B)** Step2: Identification of individual cells at different time points based on the unique mosaic color labels of cells and their respective neighboring cells. One example for each of the planes 2 and 4 is marked by white stars. **(C)** Step3: Representative quantification of the angular position of an individual cell relative to the hearts' midline. **(D)** Step4: Representative example for the calculation of the angular shift for cell number 1 on plane 1 and cell number 1 on plane 6 for the specific time window between 40-54 hpf, and comparison of the angular shifts between section planes 1 and 6 based on this representative cell. The angular shift of individual cells on each plane is calculated and averaged before intra-plane comparisons are performed (see Table S2B). Related to Fig. 1.

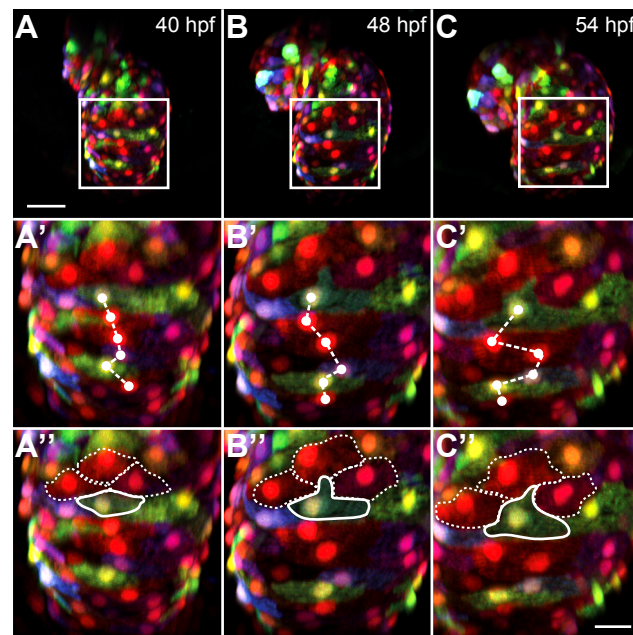


Fig. S2. Dynamic cell movements of myocardial cells during asymmetric ballooning of the heart chambers. (A-C) Reconstructions of confocal z-scan images taken from a time series (40-54 hpf). *In vivo* multi-color mosaic-labeling was performed via 1-4 cell stage injections of *myl7:RFP-T* (false-colored green) and *myl7:BFP* (blue) plasmids into *Tg(myI7:EGFP)^{twu34}* transgenic zebrafish (false-colored red). (A'-C'') Enlarged insets from A-C (white boxes). Shown are dynamic cellular (A'-C') rearrangements and (A''-C'') intercalations of myocardial cells during cardiac S-looping stages. Scale bars: (A-C) 50 μ m; (A'-C'') 20 μ m. Related to Fig. 2.

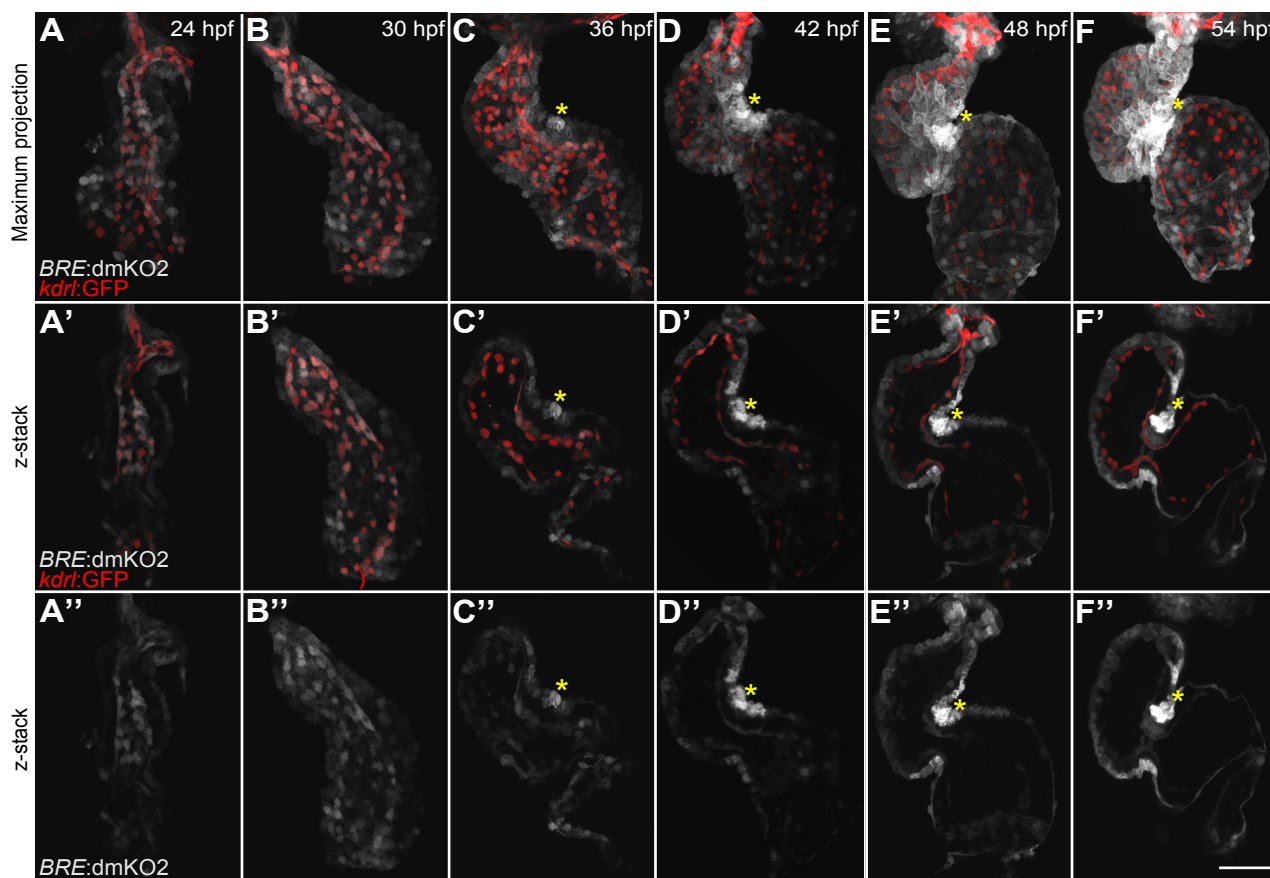


Fig. S3. Bmp signaling activity is asymmetric during S-looping morphogenesis. (A-F) Reconstructions of confocal z-stacks of representative hearts of the Bmp signaling *Tg(BRE:dmKO2)^{mw40}* (false-colored gray) and myocardial *Tg(mly7:EGFP)^{twu34}* (false-colored red) reporter lines (maximum projections). (C) At 36 hpf, *Tg(BRE:dmKO2)^{mw40}* expression is more prominent at the superior myocardial AVC (yellow asterisk). (D-F) Until 54 hpf, the intensity of this expression at the superior AVC increases (yellow asterisk). (A'-F'') For better visualization of BMP activity, z-stack images from z-scans (A-F) are shown. Yellow asterisks show myocardial regions where Bmp signaling intensities are high. Scale bars: (A-F'') 50 μ m. Related to Fig. 3.

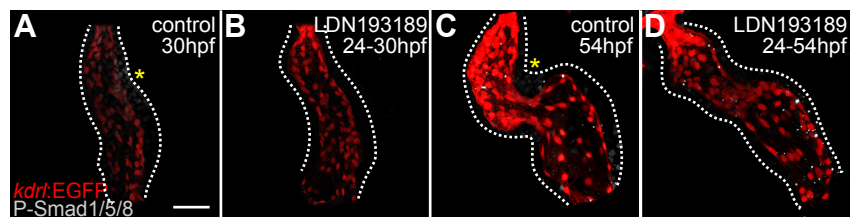


Fig. S4. Pharmacological inhibition of Bmp signaling impairs cardiac looping morphogenesis. (A,C) Reconstructions of confocal z-stacks of representative wild-type hearts immunolabeled against P-Smad1/5/8 (false-colored gray) and expressing EGFP (false-colored red) within endocardial cells. (A) At 30 hpf, P-Smad1/5/8 immunostaining is prominent at the superior myocardial AVC (yellow asterisk). (C) This asymmetry in P-Smad1/5/8 immunostaining levels is even more prominent at 54 hpf (yellow asterisk at the superior AVC). **(B,D)** Pharmacological inhibition of Bmp signaling using the inhibitor LDN193189 (20 μ M) between (B) 24-30 hpf or (D) 24-54 hpf abolishes myocardial P-Smad1/5/8 immunostaining and results in defective cardiac looping. Scale bars: (A-D) 50 μ m. Related to Fig. 3.

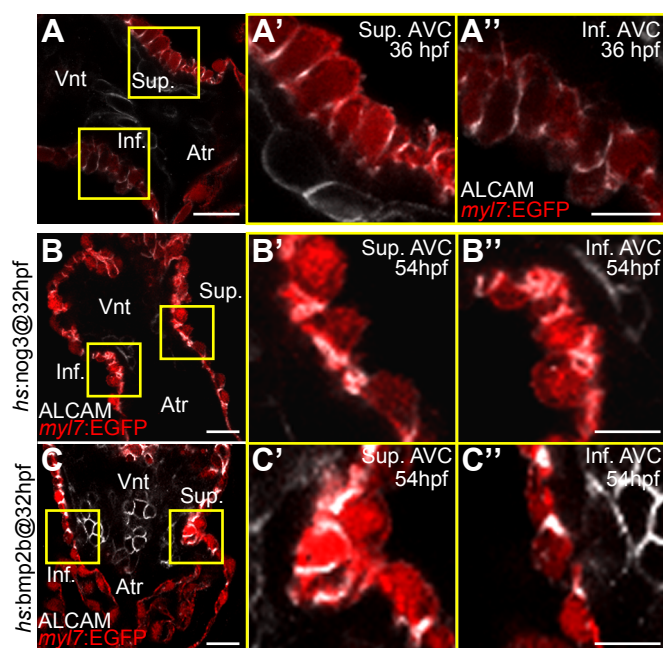


Fig. S5. Comparisons of myocardial cell morphologies within superior and inferior AVC. (A-C) Shown are single z-stack section images of ALCAM immune-labeling (marking cell borders, false-colored white) and $Tg(myI7:EGFP)^{twu34}$ myocardial reporter expression (false-colored red) in representative hearts. (A) WT heart at 36hpf; (B) Noggin3-over-expressing heart [$Tg(hsp70I:Nog3)^{fr14}$ transgenic line termed *hs@noggin3*]; and (C) Bmp2B-over-expressing heart [$Tg(hsp70:Bmp2b)^{fr13}$ transgenic line termed *hs@bmp2b*]. (B,C) Heat shocks were performed at 32 hpf and hearts recorded at 54hpf. (A'-C'') Shown are enlarged insets of superior (A'-C') and inferior (A''-C'') AVC regions from A-C (yellow boxes). At 36hpf, myocardial cells at the inferior and superior AVC have a similar rectangular shape. Down-regulation or over-activation of Bmp signaling results in abnormal myocardial cell shapes at 54 hpf. Atr, atrium; Vnt, ventricle; Sup., superior AVC; Inf., inferior AVC. Scale bars: (A-C) 20 μ m; (B'-C'') 10 μ m. Related to Fig. 3.

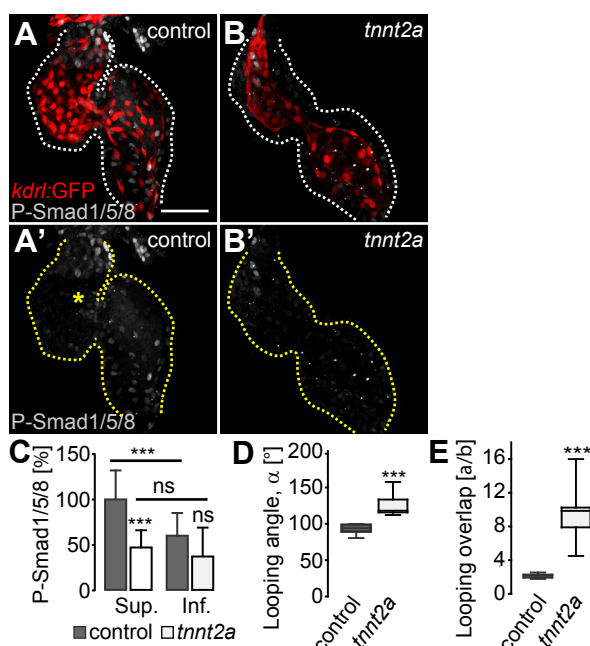


Fig. S6. Asymmetric Bmp signaling activity is lost under conditions with a lack of cardiac contractility. (A-B) Shown are reconstructions of confocal z-stacks of representative hearts at 54 hpf in (A) WT or (B) *tnnt2a* mutant embryos with endothelial *Tg(kdr1:EGFP)^{s843}* reporter expression (false-colored red) and P-Smad1/5/8 immunostaining (false-colored gray). (A'-B') Show P-Smad1/5/8 immunostaining (false-colored gray) in (A') WT and (B') *tnnt2a* mutant hearts. Outlines of hearts are delineated by yellow dotted lines. Asymmetric Bmp signaling activity within the superior AVC is indicated by yellow asterisk (A'). Summarized are quantifications of (C) relative P-Smad1/5/8 immunolabeling at the superior (Sup.) and inferior (Inf.) AVC (data in Table S6), (D) looping angle (α) (data in Table S1), and (E) index a/b (data in Table S1) in *tnnt2a* mutant vs WT hearts. Upon loss of cardiac contractility, Bmp signaling is low and homogeneously expressed within the myocardium. This corresponds with a failure of the hearts to undergo looping morphogenesis. Related to Fig. 5.

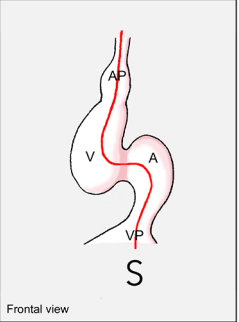
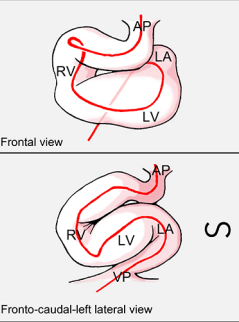
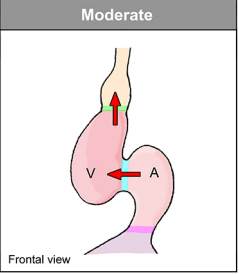
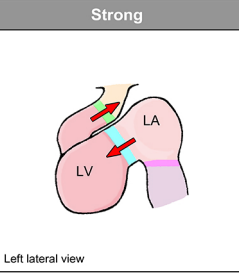
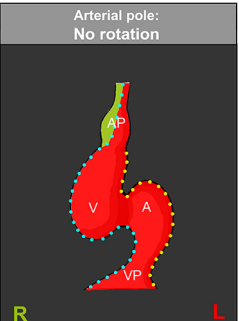

Differences in cardiac looping	
zebrafish	higher vertebrates (birds, mammals)
1 Composition of the linear heart tube	
atrial + ventricular components	ventricular component only
2 Dorsal mesocardium	
Lack of a dorsal mesocardium	Presence of a dorsal mesocardium suspected to contribute to ventricular bending + rightward rotation
3 3-D configuration of the "S-shaped" heart loop	
Planar S-loop	Complex helical S-loop
 <p>Frontal view</p>	 <p>Frontal view Fronto-caudal-left lateral view</p>
4 Extent of ventricular descent - atrial ascent	
Moderate	Strong
 <p>Frontal view</p>	 <p>Left lateral view</p>
5 Rightward "rotation"	
Arterial pole: No rotation	Arterial pole: No rotation
 <p>R L</p>	 <p>R L R L</p>
Venous pole + atrium: 90° Rotation	Venous pole + atria: No rotation

Fig. S7. Diagram depicting five fundamental differences in looping morphogenesis of the embryonic heart between zebrafish and higher vertebrates (birds and mammals).

(1) Composition of the linear heart tube. The linear heart tube of zebrafish consists of atrial and ventricular components. The linear heart tube of higher vertebrate embryos consists only of a ventricular component (embryonic left ventricle). **(2) Dorsal mesocardium.** In contrast to the zebrafish heart tube, the tubular heart of higher vertebrates has a dorsal mesocardium, which may contribute to looping morphogenesis (Linask et al., 2005; Taber et al., 1995). **(3) Geometric configuration of the S-shaped heart loop.** Zebrafish form an almost planar S-loop with bends in a frontal body plane (original mid-sagittal plane of the heart). There is only little torsion within the developing ventricle (see present data) and at the outflow tract. The S-looping of higher vertebrate embryos has a complex “two-handed helical” configuration (Männer, 2013). **(4) “Ventricular descent”/“atrial ascent”.** In all vertebrates, S-looping is characterized by a change in the positional relationship between the developing atria and ventricles along the cranio-caudal body axis, which we refer to as “ventricular descent or atrial ascent”. In zebrafish, there is only a moderate ventricular descent/atrial ascent, which positions the ventricular outflow region close to the atrial inflow region. As a consequence, the ventricular flow pathway (red arrows) makes a roughly 90° turn from the AVC (marked in light blue) to the level of the future aortic valve (marked in green). In higher vertebrates, ventricular descent/atrial ascent places the developing ventricles caudal to the developing atria. As a consequence, the ventricular flow pathway (red arrows) makes a roughly 180° turn from the AVC to the level of the future aortic valve. **(5) Rightward “rotation”.** In all vertebrates, the ventricular component of the looping heart tube undergoes rightward “rotation”. This results in the left-heart-field myocardium (marked red) forming the ventral wall and the right-heart-field myocardium (marked green) forming the dorsal wall of the looped ventricular bend. In zebrafish, rightward rotation is not confined to the developing ventricle but includes the developing atrium and the venous heart pole (Noel et al., 2013). In higher vertebrates, rightward rotation is confined to the developing ventricles (Männer, 2009) generating torsions within the components that connect the ventricular loop with the atrium (AVC) and the aortic sac (outflow tract). A: developing atrium; AP: arterial heart pole; AVC: atrioventricular canal; LA: developing left atrium; LV: embryonic left ventricle; RA: developing right atrium; RV: embryonic right ventricle; V: developing ventricle; VP: venous heart pole.

REFERENCES

- Linask, K. K., Han, M., Cai, D. H., Brauer, P. R. and Maisastry, S. M.** (2005). Cardiac morphogenesis: matrix metalloproteinase coordination of cellular mechanisms underlying heart tube formation and directionality of looping. *Dev Dyn* **233**, 739-53.
- Männer, J.** (2009). The anatomy of cardiac looping: a step towards the understanding of the morphogenesis of several forms of congenital cardiac malformations. *Clin Anat* **22**, 21-35.
- Männer, J.** (2013). On the form problem of embryonic heart loops, its geometrical solutions, and a new biophysical concept of cardiac looping. *Ann Anat* **195**, 312-23.
- Noel, E. S., Verhoeven, M., Legendijk, A. K., Tessadori, F., Smith, K., Choorapoikayil, S., den Hertog, J. and Bakkers, J.** (2013). A Nodal-independent and tissue-intrinsic mechanism controls heart-looping chirality. *Nat Commun* **4**, 2754.
- Stainier, D. Y., Lee, R. K. and Fishman, M. C.** (1993). Cardiovascular development in the zebrafish. I. Myocardial fate map and heart tube formation. *Development* **119**, 31-40.
- Taber, L. A., Lin, I. E. and Clark, E. B.** (1995). Mechanics of cardiac looping. *Dev Dyn* **203**, 42-50.